

A SURVEY OF O VI, C III, AND H I IN HIGHLY IONIZED HIGH-VELOCITY CLOUDS

ANDREW J. FOX¹, BLAIR D. SAVAGE, & BART P. WAKKER

Department of Astronomy, University of Wisconsin - Madison, 475 North Charter St., Madison, WI 53706

Draft version November 4, 2018

ABSTRACT

We present a *Far-Ultraviolet Spectroscopic Explorer* survey of highly ionized high-velocity clouds (HVCs) in 66 extragalactic sight lines with $S/N_{1030} > 8$. We searched the spectra for high-velocity ($100 < |v_{LSR}| < 400 \text{ km s}^{-1}$) O VI absorption and found a total of 63 absorbers, 16 with 21 cm-emitting H I counterparts and 47 “highly ionized” absorbers without 21 cm emission. The highly ionized HVC population is characterized by $\langle b(\text{O VI}) \rangle = 38 \pm 10 \text{ km s}^{-1}$ and $\langle \log N_a(\text{O VI}) \rangle = 13.83 \pm 0.36$, with negative-velocity clouds generally found at $l < 180^\circ$ and positive-velocity clouds found at $l > 180^\circ$. 11 of these high-velocity O VI absorbers are positive-velocity wings (broad O VI features extending asymmetrically to velocities of up to 300 km s^{-1}). We find that 81% (30/37) of high-velocity O VI absorbers have clear accompanying C III absorption, and 76% (29/38) have accompanying H I absorption in the Lyman series. We present the first (O VI-selected) sample of C III and H I absorption line HVCs, and find $\langle b(\text{C III}) \rangle = 30 \pm 8 \text{ km s}^{-1}$, $\log N_a(\text{C III})$ ranges from 12.8 to > 14.4 , $\langle b(\text{H I}) \rangle = 22 \pm 5 \text{ km s}^{-1}$, and $\log N_a(\text{H I})$ ranges from 15.1 to > 16.9 . The lower average width of the high-velocity H I absorbers implies the H I lines arise in a separate, lower temperature phase than the O VI. The ratio $N_a(\text{C III})/N_a(\text{O VI})$ is generally constant with velocity in high-velocity O VI absorbers, suggesting that C III resides in the same gas as the O VI. Collisional ionization equilibrium models with solar abundances can explain the O VI/C III ratios for temperatures near $1.7 \times 10^5 \text{ K}$; non-equilibrium models with the O VI “frozen-in” at lower temperatures are also possible. Photoionization models are not viable since they under-predict O VI by several orders of magnitude. The presence of associated C III and H I strongly suggests the high-velocity O VI absorbers are not formed in the hotter plasma that gives rise to O VII and O VIII X-ray absorption.

We find that the shape of the O VI positive-velocity wing profiles is well reproduced by a radiatively cooling, vertical outflow moving with ballistic dynamics, with $T_0 = 10^6 \text{ K}$, $n_0 \approx 2 \times 10^{-3} \text{ cm}^{-3}$, and $v_0 \approx 250 \text{ km s}^{-1}$. However, the outflow has to be patchy and out of equilibrium to explain the sky distribution and the simultaneous presence of O VI, C III, and H I. We found that a spherical outflow can produce high-velocity O VI *components* (as opposed to the wings), showing that the possible range of outflow model results is too broad to conclusively identify whether or not an outflow has left its signature in the data. An alternative model, supported by the similar multi-phase structure and similar O VI properties of highly ionized and 21 cm HVCs, is one where the highly ionized HVCs represent the low $N(\text{H I})$ tail of the HVC population, with the O VI formed at the interfaces around the embedded H I cores. Though we cannot rule out the possibility that some high-velocity O VI absorbers exist in the Local Group or beyond, we favor a Galactic origin. This is based on the recent evidence that both H I HVCs and the million-degree gas detected in X-ray absorption are Galactic phenomena. Since the highly ionized HVCs appear to trace the interface between these two Galactic phases, it follows that highly ionized HVCs are Galactic themselves. However, the non-detection of high-velocity O VI in halo star spectra implies that any Galactic high-velocity O VI exists at z -distances beyond a few kpc.

Subject headings: Galaxy: halo – intergalactic medium – ISM: clouds – ultraviolet: ISM – ISM: kinematics and dynamics

1. INTRODUCTION

The *Far-Ultraviolet Spectroscopic Explorer* (*FUSE*) survey of O VI in the Galactic halo and high-velocity clouds (HVCs; Wakker et al. 2003; Savage et al. 2003; Sembach et al. 2003, hereafter S03) found that high-velocity ($|v_{LSR}| > 100 \text{ km s}^{-1}$) O VI is detected with a strength $W_\lambda > 30 \text{ mÅ}$ in 70% of sight lines across the entire sky. These absorbers trace gas created by a variety of processes. The high-velocity O VI associated with known high-velocity H I structures (Complexes A and C, and the Magellanic Stream) has been well studied (S03, Fox et al.

2004, 2005). In these cases, the O VI observations are best explained by conductive or turbulent interfaces, where hot gas exists in transition-temperature boundary layers between the cool/warm H I HVCs and a surrounding hot ($\sim 10^6 \text{ K}$) medium. In other high-velocity O VI absorbers, no H I 21 cm emission is detected at the same velocity as the O VI; these absorbers are referred to as highly ionized HVCs (Sembach et al. 1995, 1999; Collins et al. 2004, 2005; Ganguly et al. 2005). Ultraviolet (UV) and far-UV observations are required to detect and study the material in highly ionized HVCs. A particular category of highly ionized HVC first described in S03 is the positive-velocity wing – a broad feature extending asymmetrically to velocities of up to $+300 \text{ km s}^{-1}$ with-

¹ Current address: Institut d’Astrophysique de Paris, 98 bis, Boulevard Arago, 75014, Paris, France

out corresponding absorption at negative velocity. Wings appear to be a continuation of low-velocity Milky Way absorption, rather than discrete absorption components. Their nature and origin is currently unknown.

One interpretation of the O VI wings (and potentially other high-velocity O VI absorbers) is that they trace a hot Galactic wind or fountain. In this scenario, activity in the Galactic disk (Type II supernovae, massive star stellar winds, and possibly AGN activity) creates large volumes of hot, pressurized interstellar gas that rises upward into the halo. At low outflow speeds, the material will fall back to the plane as a fountain (Shapiro & Field 1976; Bregman 1980; Houck & Bregman 1990). A faster outflow (a wind) can escape the Galactic potential well, in doing so transporting mass, metals, and energy to the intergalactic medium (see review by Veilleux, Cecil, & Bland-Hawthorn 2005). In our own galaxy, mid-infrared images of the Galactic center show a large-scale bipolar outflow (Bland-Hawthorn & Cohen 2003). A lack of neutral hydrogen above $z \approx 1$ kpc in the inner 3 kpc of the Milky Way (Lockman 1984) supports the idea of a wind, since the H I could have been expelled or ionized. O VI-containing outflows are predicted by hydrodynamical simulations of galaxy winds (Mac Low & Ferrara 1999; Strickland & Stevens 2000), and have been detected in starburst galaxies NGC 1705 (Heckman et al. 2001) and NGC 625 (Cannon et al. 2004). Although these extragalactic absorbers exist in the form of discrete components, not wings, they may appear to resemble wings when observed from inside the galaxies. However, a hot Milky Way outflow has never been conclusively detected in the ultraviolet, but if present should be detectable in O VI absorption in the spectra of distant quasars.

Alternatively, many high-velocity O VI absorbers may arise at large distances, rather than being associated with the Milky Way. The possibility of large quantities of hot plasma pervading the Local Group has gained attention due to several detections of zero redshift absorption in the X-ray lines of O VII and O VIII (e.g. Nicastro et al. 2002; Fang et al. 2003; McKernan, Yaqoob, & Reynolds 2004; Williams et al. 2005; Williams, Mathur, & Nicastro 2006). This hot gas is likely tracing either the Warm-Hot Intergalactic Medium (WHIM), or an extended Galactic corona (S03). In the WHIM interpretation, the X-ray observations represent the detection of a warm-hot phase predicted by large-scale cosmological simulations (Cen & Ostriker 1999; Davé et al. 2001). Such a phase would contain a considerable fraction of the baryons at the current epoch (see Nicastro et al. 2002; Nicastro 2005). However, the hot extended corona interpretation is favored by observations of interstellar O VII absorption toward X-ray binaries in a Galactic globular cluster (Futamoto et al. 2004) and in the LMC (Wang et al. 2005).

In this paper we extend the S03 survey by focusing on the highly ionized HVCs, and looking for absorption in C III and H I accompanying the high-velocity O VI. We use a new decontamination technique for removing the effects of interstellar H₂ (Wakker 2006), and include new data taken with the *FUSE* satellite up to December 2004. The scientific motivation for this extension is to understand the origin of the positive-velocity wings, and the highly ionized HVCs in general.

Section 2 describes our observations and data reduction. In §3 we describe the measurement of high-velocity absorption, present column densities for O VI, C III, and H I, and display the spectra. In §4 we analyze our results, looking at kinematics and the distribution of high-velocity O VI on the sky, distance information, ionization, and the relationship between absorption in different species. Section 5 contains a comparison of the properties of high-velocity absorbers with the predictions of origin models. Our work is summarized in §6.

2. OBSERVATIONS AND DATA HANDLING

2.1. Data Reduction

Our far-UV spectra were obtained between the years 2000 and 2005 using the *FUSE* satellite (Moos et al. 2000; Sahnow et al. 2000). For wavelengths below 1000 Å (C III and H I lines), we use data from the SiC2A detector segment. For wavelengths between 1000 and 1100 Å (O VI lines), we use combined LiF1a and LiF2b data.

We extracted from the *FUSE* archives spectra of all extragalactic sight lines publically available in May 2005 with signal-to-noise per resolution element at 1030 Å ($S/N_{1030} > 8^2$). This produced a list of 88 sight lines. We did not include absorbers that may be present in data with $S/N_{1030} < 8$, since apparent column density measurements in data that noisy tend to be overestimated (Fox, Savage, & Wakker 2005), and the H₂ absorption is difficult to model (Wakker 2006). The raw sample contains 55 directions at $b > 0^\circ$, and 33 directions at $b < 0^\circ$. A general absence of sources in the range $|b| < 20^\circ$ is due to high extinction in these directions.

For each sight line the data were reduced with the calibration pipeline CALFUSE v2.1 or v2.4, with a further velocity zero-point shift for each segment and for each exposure determined and applied as described in Wakker (2006). Since only marginal improvement in the calibration results from using v2.4 rather than v2.1, the recalibration of all datasets with a common pipeline version was deemed unnecessary.

Continua were fit near the lines of interest (O VI $\lambda 1031.926$, C III $\lambda 977.020$, and the H I Lyman lines) using Legendre polynomials. In cases where O I* airglow emission is strong near 0 km s⁻¹ in C III $\lambda 977.020$, we use the night-only data for this line. Night-only *FUSE* data is always used when measuring the H I absorption in the $\lambda 972.537$, $\lambda 949.743$, $\lambda 937.804$, and $\lambda 930.748$ lines, unless the S/N in the night-only data is so poor that no useful measurement is possible.

2.2. H₂ Decontamination

We applied a H₂ modelling procedure to the *FUSE* data, using all available lines from the Lyman and Werner bands (for a full description of this process, see Wakker 2006). The process characterizes each component of H₂ absorption with six parameters: central velocity, line width, total H₂ column density, and three excitation temperatures that together give the relative populations for rotational levels $J=0$ to 4. This model is used to produce a new continuum with the effects of

² The S/N is measured by calculating the rms dispersion around the fitted continuum using data rebinned to pixels equal in size to the resolution element (20 km s⁻¹).

H_2 removed. In cases where multiple components of H_2 absorption exist, each component is fitted separately.

Of particular note in this study are the H_2 (6–0) P(3) and (6–0) R(4) lines at 1031.191 and 1032.356 Å, respectively. These features lie at -214 and $+123$ km s $^{-1}$ in the frame of O VI $\lambda 1031.926$, and so could mimic the effect of high-velocity O VI absorption. The precision of our $N(O\text{ VI})$ measurements is thus limited by the quality of the H_2 modelling, with the error on $N(O\text{ VI})$ including a systematic contribution from the uncertainty on the H_2 model.

2.3. Removal of Contaminated Spectra

We omitted 22 sight lines where we have no information on the presence of HVCs in absorption in O VI $\lambda 1031.926$. The reasons for this were: blends with intrinsic or intergalactic absorption line systems, highly uncertain continuum placement, or complicated H_2 lines that could not be reliably modelled. Table 1 contains a list of the 66 remaining sight lines, together with a summary of their basic information.

2.4. Identification of Highly Ionized HVCs and H I HVCs

We searched the spectra in the sample for high-velocity absorption in O VI $\lambda 1031.926$, defined in the range $100 < |v_{LSR}| < 400$ km s $^{-1}$, and found 49/66 sight lines showed high-velocity O VI detections. O VI absorption in the range -100 to 100 km s $^{-1}$ is usually attributed to the Galactic “thick disk” (Savage et al. 2003), whereas O VI absorption in the range $400 < |v_{LSR}| < 1000$ km s $^{-1}$ is rare, and appears to be associated with external galaxies (S03). In most cases O VI $\lambda 1037.617$ was not useful for studying high-velocity O VI due to blends with C II $\lambda 1036.337$, C II* $\lambda 1037.018$, $H_2 \lambda 1037.149$, and $H_2 \lambda 1038.157$.

Since the O VI associated with 21 cm H I-emitting HVCs has been well studied, we then excluded from our survey 16 high-velocity O VI absorbers clearly associated (both spatially and kinematically) with Complex A, Complex C, the Outer Arm, or the Magellanic Stream. For the purpose of this exercise, the 2×10^{18} cm $^{-2}$ H I 21 cm contour (Hulsbosch & Wakker 1988) was used to define the edge of the HVCs, and any high-velocity O VI absorbers seen in sight lines passing through these clouds at the velocity of the H I HVC were judged to be associated with the H I HVC. The sight lines with excluded absorbers are not discarded, since they contain valuable information on O VI absorption (or lack thereof) at other velocities.

The sky distribution of our sample can be seen in Figure 1, showing the high-velocity O VI sky at both negative and positive velocities. The circle size is scaled by the O VI column density in the high-velocity absorber (see §3 for a description of how $N(O\text{ VI})$ is measured).

2.5. Incidence of High-velocity O VI Absorption

- High-velocity O VI absorption appears in 74% (49/66) of extragalactic *FUSE* spectra with S/N > 8 . This compares to the findings of S03 who detected high-velocity O VI in 84% (84/100) of extragalactic sight lines (including lower S/N data).

- 23% (15/66) of sight lines show high-velocity O VI with 21 cm H I counterparts. These are the “regular” HVCs with $\log N(\text{H I}) \gtrsim 18.2$.
- 52% (34/66) of sight lines show high-velocity O VI with no 21 cm H I counterparts. These are the highly ionized HVCs.
- 26% (17/66) of sight lines show no detections of high-velocity O VI.
- In the 15 sight lines showing O VI absorption associated with 21 cm emitting clouds, 16 high-velocity O VI components are found. ESO265-G23 is the single case where there appear to be two high-velocity O VI components, in the velocity range of the Magellanic Stream.
- In the 34 sight lines showing highly ionized O VI, a total of 47 highly ionized HVCs are found (20 North and 27 South, 30 at positive velocity and 17 at negative velocity; 22 sight lines show one high-velocity O VI absorber, 11 sight lines show two, and one sight line shows three).
- Approximately three out of four high-velocity O VI absorbers are highly ionized, i.e. do not have 21 cm counterparts.
- Since there could be highly ionized O VI masking behind O VI associated with 21 cm HVCs, the number of uncontaminated sight lines in which to look for highly ionized HVCs is $66 - 15 = 51$. Thus, the corrected incidence of highly ionized HVCs is 47 in 51 sight lines with no high-velocity H I 21 cm emission (0.92 highly ionized HVCs per sight line).

Our sample of highly ionized HVCs is biased by the exclusion of absorbers centered in the range $|v_{LSR}| < 100$ km s $^{-1}$, and by the removal of velocity ranges in directions showing strong HVC 21 cm emission. Many of the sight lines were also originally selected to be observed based on a low $N(\text{H I})$, for low extinction; this produces a separate observational bias.

3. MEASUREMENT OF ABSORPTION

We used the apparent optical depth (AOD) method (Savage & Sembach 1991; Sembach & Savage 1992) to measure the apparent column densities of O VI, C III, and H I absorption in the O VI HVCs. This technique requires no prior knowledge about the component structure and is valid for measurement of velocity-resolved, unsaturated lines. The high-temperature environments in which O VI is thought to exist ensure that the O VI lines have enough thermal broadening to be resolved. Saturation can be checked for using the weaker O VI line, but numerous blends at high-velocity prevent the assessment being made in our dataset. Savage et al. (2003) demonstrated that saturation was generally not a problem for the thick-disk O VI absorption in a similar-sized *FUSE* dataset that included many of the same sight lines we study here; by association, the high-velocity O VI in our survey, which is generally weaker than the thick-disk O VI, is likely unsaturated too.

The main spectroscopic measurements for sight lines with high-velocity O VI detections are presented in Table 2. For each sight line we list the range of high-velocity absorption (identified by eye using the O VI line), then for O VI, C III, and H I we list the central velocity v_0 , line width b , equivalent width W_λ in the velocity range v_- to v_+ , apparent column density N_a between v_- and v_+ , and detection significance, defined as $W_\lambda/\sigma(W_\lambda)$. For H I, the Lyman series absorption line chosen to make the measurement is listed. This choice is made by finding a relatively weak line free from airglow and blends. For cases where high-velocity O VI is seen with no counterpart in C III or in H I, we present 3σ upper limits to $\log N$ in these species, using the 3σ equivalent width limit in the same velocity integration range used for O VI, and a linear curve-of-growth. In Table 3 we list those sight lines and velocity ranges without high-velocity O VI detections and the corresponding 3σ upper limits for $N(\text{O VI})$.

Measuring $N(\text{H I})$ in the high-velocity absorbers is much more challenging than measuring O VI, for the following reasons: (1) Noisy data in the SiC channels: we find S/N_{970} is typically $0.5S/N_{1030}$. (2) Saturation: many high-velocity absorbers are saturated through the weakest Lyman line observable with *FUSE* ($\text{H I } \lambda 917.181$). (3) Blending: contamination arises from a high concentration of H_2 , O I, and other lines. (4) Atmospheric emission: airglow is seen near 0 km s^{-1} in the stronger Lyman lines. The airglow, which can be reduced but not fully removed by using night-only rather than combined day+night data, leads to a shortage of information on the shape of the interstellar line profile in the range $|v_{\text{LSR}}| \lesssim 100 \text{ km s}^{-1}$. (5) Difficulties in continuum placement: the high density of absorption lines at $\lambda < 1000 \text{ \AA}$ results in a lack of spectral regions free from absorption, needed to place the continuum. (6) Assuming the H I lines are resolved: the AOD technique can only be applied to lines that are resolved, otherwise the column densities will be underestimated. If the H I exists in cool gas at $T < 1.4 \times 10^4 \text{ K}$ and has no non-thermal broadening, the Lyman lines will not be resolved by the *FUSE*/SiC channels, and then full saturation could be hidden. For these reasons, the uncertainty on $N(\text{H I})$ is much larger than on $N(\text{O VI})$ or $N(\text{C III})$. However, even without precise measurements of $N(\text{H I})$, we can still make an assessment of whether H I absorption is present at the velocity of the O VI absorption.

Plots showing the O VI, C III, and H I absorption for all the highly ionized HVCs are presented in Figure 2. We classified each absorber into one of three categories based on the properties of the high-velocity O VI absorber: positive-velocity wings (broad absorption blending with the thick disk at $|v_{\text{LSR}}| < 100 \text{ km s}^{-1}$ and continuing out up to 300 km s^{-1}), positive-velocity components (isolated absorption components), and negative-velocity components. No negative-velocity wings were observed. Summary plots showing O VI, C III, and H I for all absorbers in each category are displayed in Figures 3 to 5. In Figure 6 we include all high-velocity O VI non-detections, together with the profiles of those O VI absorbers excluded from our survey (those associated with 21 cm H I-emitting HVCs).

4. ANALYSIS

4.1. Distribution of Highly Ionized HVCs on the Sky

Table 4 contains analysis of the properties and sky distribution of highly ionized high-velocity O VI absorbers. In Figure 7 we show the distribution of absorber velocities with longitude and latitude, in both the Local Standard of Rest (LSR) and Galactic Standard of Rest (GSR) reference frames ($v_{\text{GSR}} = v_{\text{LSR}} + (220 \text{ km s}^{-1}) \sin l \cos b$). The overall distribution has a marked dipole appearance, as evidenced by the following:

- 82% of negative-velocity highly ionized HVCs are at $l < 180^\circ$.
- 94% of negative-velocity highly ionized HVCs are at $b < 0^\circ$.
- 73% of positive-velocity highly ionized HVCs absorbers are at $l > 180^\circ$.
- 63% of positive-velocity highly ionized HVCs absorbers are at $b > 0^\circ$.

In the following points we discuss several features of the distribution of high-velocity O VI on the sky (Figs. 1 and 7).

There is a lack of highly ionized HVCs, both at positive and negative velocities, in the quadrant $l < 180^\circ$, $b > 0^\circ$. Both selection effects and real effects appear to be at work here; these are discussed in turn in the next two points.

Two selection effects prevent the detection of highly ionized HVCs in the range $0^\circ < l < 180^\circ$, $0^\circ < b \lesssim 45^\circ$. At negative velocities the lack of detections is largely due to the exclusion of sight lines through Complex C and Complex A. There could be negative-velocity highly ionized HVCs in these directions, but we have no way of separating these absorbers from O VI absorption associated with the 21 cm-emitting structures. At positive velocities, the lack of highly ionized HVCs in this region may be related to the LSR motion around the Galactic center. For example, material moving at $v_{\text{GSR}}=100 \text{ km s}^{-1}$ along sight lines at $0^\circ < l < 180^\circ$ and low Galactic latitude would be masked, from our vantage point, by thick disk material since the solar motion is in this direction; our absorber selection procedures would therefore not identify such material as high-velocity. This argument can also explain the non-detections of highly ionized HVCs in the region $0^\circ < l < 180^\circ$, $-45^\circ \lesssim b < 0^\circ$.

There are several significant non-detections of high-positive-velocity O VI at $0^\circ < l < 180^\circ$, $b \gtrsim 45^\circ$ (e.g. Mrk 279, PG 1259+593). At higher latitude, the component of solar motion decreases, so any outflowing material in the first two quadrants will no longer be masked by rotating disk material in the foreground. The absence of high-latitude high-positive-velocity O VI absorbers at $0^\circ < l < 180^\circ$ (the Complex C sight lines) is thus an important observation, particularly because the *FUSE* data in these sight lines tend to have good S/N ratios. Mrk 817 is the only sight line showing high-positive-velocity O VI in this part of the sky³.

Many high-velocity O VI absorbers are close to the orbit of the Magellanic Stream. We note the similarity in

³ Though the Mrk 817 features (two components are seen) are weak, the spectrum has very high signal-to-noise and the 190 km s^{-1} component is also seen in O VI $\lambda 1037.617$.

kinematics and location on the sky between many high-velocity O VI absorbers and the Magellanic Stream (see Figure 1). If many high-velocity O VI absorbers were associated with the Stream, it would indicate the Stream extends further out in space than the regions sampled by H I 21 cm emission (see Fox et al. 2005, for further evidence of this conclusion). Note that the negative-velocity components seen in the range $20^\circ < l < 120^\circ$, $-60^\circ < b < -30^\circ$ and $v \approx -150$ to -100 km s^{-1} appear *unrelated* to the Magellanic Stream despite their proximity on the sky, since the Stream has velocities over 100 km s^{-1} more negative than the absorber velocities in these directions.

In sight lines close to but off the edge of 21 cm complexes, the highly ionized boundary layers appear to be fairly confined. Note the high-negative-velocity O VI non-detections in sight lines close to but a few degrees outside the H I boundaries of Complex C and the anti-center clouds (Figure 1). The O VI associated with these 21 cm-emitting complexes is therefore confined rather than extended, supporting the idea that the large complexes are surrounded by relatively narrow O VI-bearing interface layers (Fox et al. 2004). In the conductive interface models of Borkowski et al. (1990), the typical thickness of an O VI-bearing conduction front is 15 pc (or 5' for a cloud at 10 kpc).

4.2. Presence of Other Ions

Among the more important results of our survey is that approximately 80% of high-velocity O VI absorbers have clear counterparts in both C III and the H I Lyman series.⁴ In Figure 8 we display the sky distribution of HVC absorption in O VI, C III, and H I, showing the directions in which all three ions are detected over the same velocity range. The seven cases where high-velocity C III is not detected at 3σ levels are Mrk 817 (189 km s $^{-1}$ component), Mrk 421, PG 1302–102, PG 1011–040 (279 km s $^{-1}$ component), MS 0700.7+6338, HE 1143–1810 (246 km s $^{-1}$ component), and Ton S180 (251 km s $^{-1}$ component). The nine cases where high-velocity H I is not detected, namely 3C 273.0, Mrk 817 (189 km s $^{-1}$ component), Mrk 421, Mrk 1383, ESO141–G55, PG 1302–102, MS 0700.7+6338, HE 1143–1810 (246 km s $^{-1}$ component), and Ton S180 (251 km s $^{-1}$ component) are sight lines with low column density high-velocity O VI: eight of these nine absorbers have $\log N(\text{O VI})$ lower than the overall average $\log N(\text{O VI})$ of 13.87. In other words, all strong high-velocity O VI absorbers have C III and H I counterparts.

Though these are O VI-selected samples, they represent the first systematic study of C III and H I absorption in HVCs. Among the population of 14 unsaturated C III absorbers, we find $\langle b(\text{C III}) \rangle = 30 \pm 8 \text{ km s}^{-1}$; $\log N_a(\text{C III})$ ranges from 12.8 to > 14.4 . Among the population of high-velocity absorption apparently unsaturated in H I (11 absorbers), we find $\langle b(\text{H I}) \rangle = 22 \pm 5 \text{ km s}^{-1}$; $\log N(\text{H I})$ lies in the range 15.1 to > 16.9 . We show in Figure 9 histograms of v_0 , b , and $\log N$ for the O VI,

⁴ When determining the fraction of O VI absorbers with clear C III or H I counterparts, we exclude cases where blends or low-quality data prevents the assessment from being made; these cases thus do not contribute to the statistics.

C III, and H I absorbers, by absorber category (wing or component). The H I absorption line HVCs are significantly narrower, and the C III HVCs somewhat narrower, than their O VI counterparts.

Figure 10 contains scatter plots showing a comparison of the O VI properties of HVCs with the corresponding C III and H I properties. The top panels clearly show a strong kinematic correspondence between all three ions. The middle and lower panels, comparing line widths and column densities, show an interesting property: there are trends for $b(\text{C III})$ to trace $b(\text{O VI})$ (linear correlation coefficient = 0.70) and $\log N(\text{C III})$ to trace $\log N(\text{O VI})$ (linear correlation coefficient = 0.71), but $\log N(\text{H I})$ and $\log N(\text{O VI})$ are uncorrelated (linear correlation coefficient = 0.05).

4.3. Wings vs Components

23% of high-velocity O VI absorbers (and 37% of high-positive-velocity O VI absorbers) exist in the form of positive-velocity wings. The wings are always seen at positive velocity, 8/11 at $b > 0^\circ$, and all but two are found at $l > 179^\circ$ (exceptions: Mrk 509 and Mrk 817). Wings and components can each be weak or strong, with $\log N(\text{O VI})$ between 13.0 and 14.5 in both cases.

In Table 5 we look for differences in the average properties of positive-velocity wings, positive-velocity components, and negative-velocity components. The calculation of ionization properties, using the ionic ratios C III/O VI and H I/O VI, ignores cases where C III or H I is not detected. The positive-velocity components are slightly narrower and have lower average C III/O VI and H I/O VI ratios than positive-velocity wings. There is also a higher incidence of non-detections of C III and H I among positive-velocity components: wings show accompanying C III and H I at 3σ levels in 8/9 cases; positive-velocity components show C III in 13/19 cases and H I in 11/19 cases. However, apart from the likelihood of a C III or H I counterpart, none of the wing/component differences are statistically significant. Furthermore, if one considers the negative-velocity components and positive-velocity components together, then their distributions of O VI column density, width, and ionization properties become similar to those of wings.

We conclude that there is no strong evidence for a physical difference between wings and components. The similarity of the wing population to the component population can be seen in the histograms shown in Figure 9.

4.4. Comparison with Earlier Results

Our sample of 11 O VI positive-velocity wings is significantly different from the sample of 22 positive-velocity wings in S03. We find that the reported O VI features toward Mrk 876 and 3C 273.0 (125 km s $^{-1}$ component) are likely due to H₂ contamination, and the reported wings toward PG 1351+640 and PG 1259+593 are not significant at the 3σ level. We have reclassified the absorbers toward NGC 1705, 3C 273.0 (210 km s $^{-1}$ component), and Mrk 1383 as components, not wings. The S03 wings toward PG 0947+396, HS 1102+3441, PG 1001+291, Mrk 734, HE 1115–1735 and Tol 1247–232 have too low S/N to be included in our data set. Finally, we have included the wings toward PG 1011–040, NGC 625, and

NGC 5408 in data that were released after the publication of the S03 survey.

Our non-detection of high-velocity C III absorption toward Mrk 421 is in contrast to Savage et al. (2005), who claim a detection of $W_\lambda = 26 \pm 10 \text{ m}\text{\AA}$ at $60\text{--}165 \text{ km s}^{-1}$. This absorber is not included in our sample because we only consider 3σ detections.

4.5. Constraints on the Distance to Absorbing Gas

If the O VI wings (and highly ionized HVCs in general) do trace outflowing Galactic material, they should be visible in the spectra of Galactic halo stars at high z -distance. Zsargó et al. (2003) found no evidence for O VI wings in 22 sight lines passing through the Galactic halo, with the exception of HD 100340, where substantial continuum placement uncertainty allows for the possible presence of high-velocity O VI. Zsargó et al. (2003) point out that if high-velocity O VI were as common towards halo stars as it is toward extragalactic targets, it would appear in 10–12 sight lines in their sample. However, we note that if the gas that gives rise to broad, shallow absorption wings were present toward halo stars, it would be difficult to detect against the complex, undulating, hot stellar continua.

The eight lines to BD+38 2182 and Mrk 421 form an interesting case of a halo star (BD+38 2182) closely aligned with an extragalactic target (Mrk 421), both having been observed with *FUSE* (Savage et al. 2005). BD+38 2182, a B3V star at $z = 3.5 \text{ kpc}$ does not show an O VI positive-velocity wing, even though it lies $\approx 4^\circ$ away from the sight line to AGN Mrk 421, whose spectrum displays an O VI wing extending to 160 km s^{-1} . In another halo star/AGN pair, there is weak O VI wing absorption in the range 80 to 160 km s^{-1} in the spectrum of halo star HD 100340 (even allowing for molecular hydrogen at 125 km s^{-1}), but much stronger absorption is seen in this velocity range along the nearby sight line to AGN Mrk 734. Finally, vZ 1128, a globular cluster star at $z \approx 10 \text{ kpc}$, shows no high-velocity O VI absorption (Howk, Sembach, & Savage 2003).

All these indicators (shown in Figure 11), suggest the high-velocity O VI originates beyond a few kpc, though it is impossible to draw conclusions on the whole sky from a small number of cases. If the high-velocity O VI existed in an extended distribution surrounding the galaxy, the fraction of high-velocity O VI absorbers in the inner few kpc (and hence intercepted by the halo star sight lines) could be small. On the other hand, the lack of high-velocity O VI detections towards halo stars has been used to argue for an extra-galactic origin for all the high-velocity O VI clouds (Nicastro 2005).

4.6. Ionization of high-velocity O VI

Considerable work on the ionization of interstellar O VI, both in the Galactic thick disk (Savage et al. 2003; Zsargó et al. 2003) and in high-velocity clouds (Sembach et al. 2003; Fox et al. 2004, 2005; Collins et al. 2004, 2005; Ganguly et al. 2005) has led to the understanding that O VI cannot be photoionized in these environments, because the absorber sizes necessary to reproduce the observed HVC ionization pattern given the Galactic and extragalactic radiation fields are far too large to be reasonable, and inconsistent with the results from modelling the ions C II, C III, Si II, and

Si III. Collisional processes are thus thought to dominate the production of O VI (see reviews in Fox et al. 2004; Indebetouw & Shull 2004).

Without *HST* data for many of the objects in our sample, we do not have C IV and Si IV measurements to help diagnose the ionization mechanism for each individual case. However, if the absorbers are in collisional ionization equilibrium (CIE), and a solar elemental abundance pattern is assumed⁵, the integrated column density ratio $N(\text{C III})/N(\text{O VI})$ can be used to estimate the implied temperature (Sutherland & Dopita 1993). For the high-velocity absorbers in this study, these results are presented in Table 6. Typical C III/O VI ratios in wings imply $\log T = 5.23$, or $T = 1.7 \times 10^5 \text{ K}$, though since gas near these temperatures cools very quickly, we consider thermal equilibrium to be unlikely. Although CIE solutions also exist for the H I/O VI and H I/C III ratios, the lower average width of the high-velocity H I absorbers ($\langle b(\text{H I}) \rangle = 21 \pm 7 \text{ km s}^{-1}$ versus $\langle b(\text{O VI}) \rangle = 38 \pm 10 \text{ km s}^{-1}$) implies that $\log T(\text{H I}) < 4.67$, at which temperature no O VI would form, unless the gas is in a highly non-equilibrium state or is photoionized, which we have already ruled out. *Thus, the H I exists in a separate, lower temperature phase than the high-velocity O VI.* This is also suggested by the lack of correlations between $b(\text{O VI})$ and $b(\text{H I})$, and $\log N(\text{O VI})$ and $\log N(\text{H I})$, shown in Figure 10⁶. The CIE temperatures derived from the H I/O VI (and also C III/H I) ratios then becomes meaningless.

More detailed information on ionization is provided by looking at the apparent column density ratios as a function of velocity, rather than the integrated values. This approach is problematic for ions with markedly different atomic weights and thermal broadening, but valid for O VI and C III. We have derived $N_a(\text{C III})/N_a(\text{O VI})$ ratios as a function of velocity in our highly ionized absorbers, for a selection of positive-velocity wings, positive-velocity components, and negative-velocity components (Figure 12). In each category of high-velocity O VI absorber, $N_a(\text{C III})/N_a(\text{O VI})$ ranges between 0 and 4. *In general, there is no evidence for a slope in $N_a(\text{C III})/N_a(\text{O VI})$ with velocity*, lending support to the idea that the O VI and C III ions reside in the same gaseous phase. In a few cases (both wings and components) some peaks in the ratio are seen, indicating relative enhancements of C III. Such enhancements could be due to a photoionized C III component existing in addition to a collisionally-ionized component, or alternatively from a lower-temperature C III component associated with the H I.

5. WING ORIGIN MODELS

5.1. Galactic Outflows

O VI outflows are seen in galaxies NGC 1705 (Heckman et al. 2001) and NGC 625 (Cannon et al. 2004). The idea that the O VI positive-velocity wings may trace an analogous Milky Way outflow has been sug-

⁵ We adopt $A_O^\odot = (n_O/n_H)_\odot = 10^{-3.34}$ (Asplund et al. 2004), and $A_C^\odot = (n_C/n_H)_\odot = 10^{-3.61}$ (Allende Prieto, Lambert, & Asplund 2002).

⁶ Danforth & Shull (2005) and Danforth et al. (2006) found similar evidence for multiple gas phases in their studies of O VI, C III, and H I in the low-redshift intergalactic medium.

gested before (Sembach et al. 2001, S03). In this section we explore the outflow hypothesis by developing one-dimensional models to determine the O VI absorption line profile expected in a Galactic outflow. We develop some useful insights into the expected absorption line signature of a Galactic outflow without a full hydrodynamical treatment (for which we refer the reader to Houck & Bregman 1990).

We consider outflows rather than inflows or rotating halos, since these other models have been shown to have difficulties explaining the O VI observations. S03 showed that models of a co-rotating or static halo do not explain the kinematics of the high-velocity O VI absorbers, and infalling material (Collins et al. 2005) cannot explain the numerous positive-velocity absorbers in the anti-center direction.

We derive synthetic O VI and C III column density profiles produced when looking through a uniform, radiatively cooling Galactic outflow, moving with ballistic dynamics in the Galactic gravitational field. Two geometries for the outflow are considered: vertical and spherical. Our models are calculated numerically by following the evolution of physical conditions on a grid with time interval of 1 Myr. The free parameters (initial conditions) in the models are the temperature, density, and velocity at the base of the flow (T_0 , n_0 , and v_0). To ensure a tractable problem, we restrict ourselves to the directions $l = 0^\circ$ and 180° , so that Galactic rotation does not affect the line profiles⁷⁸.

In the vertical case, the equation of motion of a parcel of gas moving vertically upward is given by $\frac{dv(z)}{dt} = -g(z)$, where we take the gravitational acceleration perpendicular to the plane from Spitzer (1978, Figure 1.7), derived using the measured z -distribution of spectral type K giants in the Galactic halo. We impose mass continuity by insisting that $v(z)n(z) = v_0 n_0 = \text{constant}$; this mass flux can be converted to a total mass flux out of the Galaxy by assuming uniform flow out of a circular disk with radius 20 kpc (i.e., assuming a covering fraction of unity).

In the radial case, we use a spherical Milky Way mass distribution truncated at $r_{max}=50$ kpc (Binney & Tremaine 1987) to determine the gravitational acceleration per unit mass: $g(r) = -v_c^2/r$ for $r < r_{max}$ and $g(r) = -v_c^2(r_{max}/r^2)$ for $r > r_{max}$. The condition of conservation of mass now becomes $r^2 n(r)v(r) = r_0^2 n_0 v_0 = \text{constant}$.

Internal energy loss in the models is through radiative cooling: $\frac{dE(z)}{dt} = -\Lambda(T[z])n_H^2(z)$ where the cooling function $\Lambda(T)$ is taken from Houck & Bregman (1990) and n_H is the total ($H^0 + H^+$) hydrogen density in cm^{-3} . Given the initial conditions, the equation of motion is solved to yield $v(z)$, which combined with mass continuity gives $n(z)$, which can be used to derive $T(z)$ using the rate of cooling. At each grid cell in our flow, we determine the fraction of atoms in the cell that are O⁵⁺ and C²⁺ $n_{O\text{ VI}}(z) = f_{O\text{ VI}}[T(z)]A_O n_H(z)$ and $n_{C\text{ III}}(z) = f_{C\text{ III}}[T(z)]A_C n_H(z)$, where $f_{O\text{ VI}}$ is the fraction

⁸ Fortunately, several observed directions (e.g. Mrk 421, PG 0953+414) lie very close to $l=180^\circ$ and have high S/N spectra.

⁸ See Collins, Benjamin, & Rand (2002) for an investigation on the effects of Galactic rotation on the ballistic motion of upward-directed clouds.

of oxygen atoms existing as O VI and A_O is the oxygen abundance (with quantities for carbon similarly defined). Here we have assumed CIE ionization distributions at each temperature, and solar oxygen and carbon abundances. The model is run until either the flow cools to 10^4 K, at which point no O VI or C III will be detectable, or the flow slows to zero, where it will blend with gas in the thick disk. Our outflow models do not include expansion cooling. In a true three-dimensional flow, the gas could expand laterally as it rises upward, doing work at the expense of internal energy. The effect of including expansion cooling, a secondary source of energy loss, would be to increase the column density of O VI at the expense of O VII. We also do not consider the effects of buoyancy, drag forces, or magnetic fields.

For a sight line at a given latitude, we interpolate the run of physical quantities with z (vertical model) or r (spherical model) onto distance along the sight line, then integrate along the sight line to obtain the predicted column density profile. We add thermal broadening by convolving the column density profile with a Gaussian having $b = (2kT/m)^{1/2}$ ($=32$ km s^{-1} for O VI at 10^6 K). The column density profiles are converted to optical depth profiles using the relation $\tau(v) = N(v)f\lambda/3.768 \times 10^{14}$, where λ is the transition wavelength in cm and f the oscillator strength of the transition⁹. In order to make our simulated observation as realistic as possible, we then generate a Gaussian thick disk O VI component, characterized by $v_0 = 0$ km s^{-1} , $b = 60$ km s^{-1} , $\log N(O\text{ VI}) = 14.34$ (Savage et al. 2003), and a central optical depth $\tau_0 = 1.1497 \times 10^{-2}N\lambda f/b$ (Spitzer 1978). We add the disk $\tau(v)$ to the outflow $\tau(v)$ to produce the total optical depth profile. The properties of C III absorption in the Galactic disk have not been fully characterized, so we proceed by using a C III disk component with identical v_0 , b , and $\log N$ as the O VI disk component. To simulate the measurement of this gas with *FUSE*, we sample the profiles onto 2.0 km s^{-1} pixels, then generate a normalized flux profile using $F_{norm}(v) = e^{-\tau(v)}$. We convolve the flux profile with a Gaussian line spread function to represent instrumental broadening by the *FUSE*/LiF spectrograph (FWHM=20 km s^{-1}). Finally, we add Poisson Noise at a (typical) level of S/N per resolution element = 12.

In Figure 13 we show the results from a typical model run. This model is parameterized by $T_0 = 10^6$ K, $n_0 = 2.0 \times 10^{-3}$ cm $^{-3}$, and $v_0 = 250$ km s^{-1} . The qualitative shape of the O VI wings can be well explained by the vertical Galactic outflow. As the gas rises, it initially maintains a high temperature and level of ionization since the rate of radiative cooling is low. When the Galactic gravitational field has slowed the flow to near zero velocity, the density rises to conserve mass, and cooling starts to occur rapidly, causing the temperature to drop to 10^4 K. These models therefore explain the observed behavior that wings are not seen at negative v_{LSR} (neglecting Galactic rotation effects). The O VI in these models traces million-degree gas rising into the halo, not gas at temperatures near 3×10^5 K where O VI peaks in abundance.

With the CIE ionization assumption, C III wings

⁹ O VI $\lambda 1031.926$, $f=0.1325$; C III $\lambda 977.020$, $f=0.7570$ (Morton 2003).

should not be seen since the flow is too hot to produce substantial quantities of C III. This prediction is clearly at odds with our detection of C III wings in 8/9 cases, so a CIE flow is ruled out. A *smooth* Galactic outflow is ruled out by the observations that wings are only seen in 14% of extragalactic sight lines, that a North/South asymmetry exists among wings, and that the Galaxy contains isolated chimneys and superbubbles releasing hot gas into the halo in local structures.

The outflow models predict a large associated column density of O VII, since they contain large columns of gas at 10^6 K and $f(\text{O VII})$ at 10^6 K is close to unity under CIE conditions. We find that $\log N(\text{O VII}) = 15 - 16$ in our vertical outflow models. For comparison, McKernan, Yaqoob, & Reynolds (2004) report five zero-redshift O VII detections at $\log N > 16.10, > 14.85, > 15.85, > 16.45$, and > 15.74 , so the model prediction (of a large reservoir of million-degree gas) is consistent with X-ray observations. However, our observation that in 81% of cases C III absorption accompanies the high-velocity O VI is inconsistent with the high-velocity O VI existing at 10^6 K in ionization equilibrium with O VII.

The outflow model has the problem of explaining why the wings are generally not seen in halo star spectra. This problem could be avoided if the outflow were initially at temperatures $\log T > 6.6$, too hot to form O VI until it reached higher z -distances. However, a higher initial temperature in turn requires a higher density, otherwise the gas will not cool to temperatures where O VI can form and a wing will not be produced. After running our models to investigate this, we found we could *not* reproduce O VI wings with high-temperature outflows. The only way to explain the halo star non-detections of high-velocity O VI with an outflow explanation is then by arguing that the O VI absorbers are being missed against complicated halo star continua, or by invoking a patchy, localized outflow. The latter argument has trouble explaining why the high-velocity O VI patchiness should be different for halo star versus AGN spectra.

The radial outflow model tends to produce narrow absorption components, whereas the vertical model produces broader absorption wings, closer to the observed O VI wings. The radial model fails to reproduce this broad absorption wings because projection effects result in the majority of the column density along a given sight line being collapsed onto a narrow range in LSR velocity. The radial models require higher initial densities and velocities to reproduce O VI features at the right v_{LSR} ; we found $n_0 \approx 2 \times 10^{-2} \text{ cm}^{-3}$ and $v_0 \approx 450 \text{ km s}^{-1}$ was necessary. A comparison of data for four high-velocity O VI absorbers with the results of the outflow modelling, showing the contrasting behavior of vertical and radial models, is presented in Figure 14. These models are all characterized by $\dot{M} \approx 10 M_{\odot} \text{ yr}^{-1}$ to each side of the Galactic plane. This total flow rate would decrease if the covering factor of the outflowing gas is < 1 .

The finding that radial outflows can produce high-velocity O VI components and vertical outflows can produce high-velocity O VI wings results makes it very difficult to interpret the data. Vertical and radial outflows are unlikely to be simultaneous, so we do not consider that outflows can explain all the highly ionized HVC observations. Therefore, while we have shown that the kin-

matics of the O VI profiles can broadly be reproduced by outflows, outflows are not demanded and we cannot determine their geometry.

5.2. Interfaces with low $N(\text{H I})$ HVCs

One explanation for the highly ionized HVCs is that they are drawn from the same population as the 21 cm-emitting H I HVCs, being those with $N(\text{H I}) < 10^{18} \text{ cm}^{-2}$. This is suggested since both highly ionized and 21 cm-bright HVCs display a multi-phase structure with H I and O VI components. The distinction between H I HVCs and highly ionized HVCs becomes merely an H I 21 cm detection limit issue: we detect 21 cm emission only when $N(\text{H I}) \gtrsim 2 \times 10^{18} \text{ cm}^{-2}$, but we intercept O VI-bearing interfaces at the front and back of the H I phase in all cases. This interpretation is supported by the observations that the high-velocity O VI velocity centroids are correlated to the high-velocity H I velocity centroids (Fig. 10) and the high-velocity O VI column densities ($\log N \approx 13 - 14$) remain the same in HVCs regardless of the presence of H I 21 cm emission. To achieve $\log N(\text{O VI}) = 13.8$, the observed average O VI column density in highly ionized HVCs, requires ≈ 6 conductive interfaces, since each interface contributes $N(\text{O VI}) \approx 10^{13} \text{ cm}^{-2}$ (Borkowski et al. 1990). Therefore some cloud fragmentation is needed to build up the observed $N(\text{O VI})$. Interfaces where the energy flow is turbulent rather than conductive are also possible (e.g. Esquivel et al. 2005).

5.3. Local Group vs Galactic Clouds

The evidence from the halo star spectra implies the $|z|$ -distance to the high-velocity O VI absorbers is $\gtrsim 10 \text{ kpc}$, and in the case of the HE 0226-4110 absorbers, metallicity and kinematic measurements suggest an association with the Magellanic Stream at $\approx 50 \text{ kpc}$ (Fox et al. 2005). However, in general, distance information is lacking for the highly ionized HVCs. An alternative explanation for the high-velocity O VI absorbers, which explains their overall kinematics, is that they form a population of distant, Local Group clouds (Nicastro et al. 2003). While we cannot rule out the possibility that some highly ionized HVCs exist in the Local Group, we favor a Galactic origin for the following reasons:

Mass. Collins et al. (2005) consider the Local Group explanation for highly ionized HVCs to be unlikely since the implied mass ($4 \times 10^{12} M_{\odot}$) is too large to be consistent with gravitational models of the Local Group.

Association with a Galactic corona. O VII absorption has been detected toward a Galactic globular cluster and toward the Large Magellanic Cloud, implying a hot, extended phase of the Galactic interstellar medium exists (Futamoto et al. 2004; Wang et al. 2005). Our finding that over 80% of highly ionized high-velocity O VI absorbers show associated C III and H I strongly suggests that the high-velocity O VI is not formed in the same gas as that producing X-ray absorption in the lines of O VII and O VIII. This conclusion is the same as that reached by Williams et al. (2005) and Williams, Mathur, & Nicastro (2006) for the high-velocity O VI in the sight lines toward Mrk 421 and Mrk 279. However, much of the high-velocity O VI could exist in interfaces between embedded clouds and the hot-

ter plasma, so the high-velocity O VI traces the corona indirectly.

Association with Galactic H I HVCs. Evidence is becoming stronger that the H I HVCs are a Galactic and not an extragalactic phenomenon (see, e.g. Pisano et al. 2004; Oosterloo 2004; Brüns et al. 2005; Richter 2006). Therefore, if H I HVCs are Galactic, and highly ionized HVCs are simply low $N(\text{H I})$ HVCs as we have argued in this paper, then highly ionized HVCs are Galactic by association.

The H I cores in the highly ionized HVCs could represent cooled clumps of tidal material stripped off nearby galaxies (e.g. the Magellanic Stream). Indeed, many highly ionized HVCs exist in the general vicinity of the Magellanic Stream (§4.1). These cores will become photoionized since the low $N(\text{H I})$ prevents any self-shielding from the ambient radiation field (Fox et al. 2005). In the future, far-UV absorption line studies could be used to extend the H I HVC distribution function to $N \ll 10^{18} \text{ cm}^{-2}$ using the Lyman series absorption lines.

6. SUMMARY

We summarize in the following points the empirical results of our survey of O VI, C III, and H I in HVCs using *FUSE* spectra of extragalactic targets with $\text{S/N}_{1030} > 8$.

1. In a sample of 66 sight lines, 49 (74%) show high-velocity O VI absorption. 15 sight lines contain O VI HVCs with H I 21 cm counterparts, and 34 sight lines contain “highly ionized” HVCs without H I 21 cm counterparts. With some sight lines containing multiple HVCs, 47 highly ionized HVCs are seen in total (20 at $b > 0^\circ$ and 27 at $b < 0^\circ$).
2. Of the negative-velocity highly ionized HVCs, 82% are at $l < 180^\circ$ and 94% are at $b < 0^\circ$. Of the positive-velocity highly ionized HVCs, 73% are at $l > 180^\circ$ and 63% are at $b > 0^\circ$.
3. We classified the highly ionized HVCs into 11 positive-velocity wings (broad O VI absorption line features extending to velocities of $200\text{--}300 \text{ km s}^{-1}$), 19 positive-velocity components (discrete absorbers), and 17 negative-velocity components. Over the whole sample, $\langle b(\text{O VI}) \rangle = 38 \pm 10 \text{ km s}^{-1}$ and $\langle \log N(\text{O VI}) \rangle = 13.83 \pm 0.36$. 81% of the high-velocity O VI absorbers have clear accompanying C III absorption at the same velocity, and 76% of cases have accompanying H I absorption in the Lyman series. The cases where high-velocity C III and high-velocity H I are not detected are almost all weak, low column density high-velocity O VI absorbers. The likelihood of a high-velocity O VI absorber having a C III or H I counterpart is unconnected to position on the sky.
4. We present the first (O VI-selected) sample of C III and H I absorption line HVCs. For the 14 unsaturated C III absorbers, we find $\langle b(\text{C III}) \rangle = 30 \pm 8 \text{ km s}^{-1}$; $\log N_a(\text{C III})$ ranges from 12.8 to > 14.4 . For the 11 unsaturated high-velocity H I absorbers, we find $\langle b(\text{H I}) \rangle = 22 \pm 5 \text{ km s}^{-1}$; $\log N_a(\text{H I})$ ranges from 15.1 to > 16.9 .
5. The upper limit on temperature provided by the average width of the high-velocity H I lines is $\log T < 4.67$, where no O VI is expected to exist. Therefore, the O VI and H I exist in separate phases of gas. HVCs are multi-phase structures.
6. Photoionization is an unlikely explanation for the high-velocity O VI, since the required cloud sizes are extremely large (S03) and inconsistent with those suggested by other ions (Fox et al. 2005). Detailed comparisons of the high-velocity O VI and C III line profiles indicate that $N_a(\text{C III})/N_a(\text{O VI})$ is generally constant with velocity in highly ionized HVCs (with a value between 0 and 4), indicating that O VI and C III may coexist in the same, collisionally ionized phase. The relative ion ratios of O VI/C III can be formed in CIE at temperatures near $1.7 \times 10^5 \text{ K}$, assuming a solar elemental abundance pattern, though the high rate of cooling at these temperatures makes CIE unlikely.
7. Positive-velocity wings represent 23% of all high-velocity O VI absorbers with no 21 cm counterparts, and are seen in 14% of all extragalactic sight lines observed with *FUSE* at $\text{S/N} > 8$. 89% of O VI wing absorbers have counterparts in C III and H I. For the population of 11 positive-velocity wings in our sample, we measure $\langle \log N_a \rangle = 13.86 \pm 0.46$, $\langle v_0 \rangle = 134 \pm 28 \text{ km s}^{-1}$, and $\langle b \rangle = 40 \pm 11 \text{ km s}^{-1}$. 8/11 wings are seen at $b > 0^\circ$, and 9/11 at $l > 179^\circ$, but wings are not seen at negative velocities. Wings are not seen toward halo stars out to $z \approx 5 \text{ kpc}$, although continuum placement is difficult in these cases. The average properties of O VI wings are statistically no different from O VI components.
8. The prevalence of C III and H I absorption kinematically associated with the high-velocity O VI rules out the idea that the high-velocity O VI is co-spatial with O VII- and O VIII-absorbing gas.

We now discuss the implications of our results on the origins of the highly ionized HVCs.

9. **Galactic Outflows.** We produced one-dimensional ballistic models of cooling, decelerating Galactic outflows to determine the O VI line profiles expected in an outflow scenario. We find that vertical (fountain) outflows originating in the disk with $T_0 = 10^6 \text{ K}$, $n_0 \approx 2 \times 10^{-3} \text{ cm}^{-3}$ and $v_0 \approx 250 \text{ km s}^{-1}$ can reproduce the kinematic line profiles of the O VI positive-velocity wings. The radial outflows produce narrower absorption components, due to projection effects from our solar vantage point. In order to explain the observations, the Galactic outflow must be patchy (to deal with the wing non-detections toward other AGNs and halo stars) and out of CIE (to account for the C III). We could not reproduce O VI wings with higher temperature ($T_0 > 5 \times 10^6 \text{ K}$) outflows since the gas cooling time is too long. While the kinematics of the O VI profiles can broadly be reproduced by outflows, outflows are not demanded and we cannot determine their geometry from the current data.
10. **Interfaces with low $N(\text{H I})$ HVCs.** Our model of highly ionized HVCs (multi-phase structures

containing an H I core, a transition-temperature boundary layer, and a hot surrounding medium) is the same as that used to explain the structure of the large 21 cm H I-emitting complexes. It therefore seems reasonable to conclude that, with the possible exception of positive-velocity wings, highly ionized HVCs represent the subset of HVCs having $N(\text{H I}) \lesssim 10^{18} \text{ cm}^{-2}$, too small to be detected in 21 cm emission. The similarity in the properties of O VI absorption in 21 cm-bright and highly ionized HVCs supports this model, as does the correlation between the high-velocity O VI velocity centroids and the high-velocity H I velocity centroids.

11. **Local Group vs Galactic Clouds.** We cannot rule out the possibility that some high-velocity O VI absorbers exist in the Local Group or beyond. However, we favor a Galactic origin based on the unreasonably high implied mass in the Local Group case (Collins et al. 2005), the recent evidence that

H I HVCs are Galactic (Oosterloo 2004) and that highly ionized HVCs are related to the H I HVCs (this paper), and the detection of a large reservoir of hot interstellar plasma around the galaxy (Wang et al. 2005) and that highly ionized HVCs can be formed in interfaces adjoining this plasma. The non-detection of high-velocity O VI in halo star spectra implies that any Galactic high-velocity O VI exists at z -distances beyond a few kpc.

Acknowledgments

We thank Marilyn Meade for assisting with the CAL-FUSE data reduction pipeline, and are grateful to the referee for a number of perceptive comments. BDS acknowledges support through NASA grant NNG04GK12G and the University of Wisconsin Graduate School. BPW was supported by NASA grants NAG5-9179 and NNG04GD85G.

Facility: FUSE

REFERENCES

Allende Prieto, C., Lambert, D. L., & Asplund, A. 2002, *ApJ*, 573, L137
 Asplund, M., Grevesse, N., Sauval, A. J., Allende Prieto, C., Kiselman, D. 2004, *A&A*, 417, 751
 Binney, J., & Tremaine, S. 1987, "Galactic Dynamics", Princeton University Press, Princeton
 Bland-Hawthorn, J., & Cohen, M. 2003, *ApJ*, 582, 246
 Borkowski, K. J., Balbus, S. A., & Fristrom, C. C. 1990, *ApJ*, 355, 501
 Bregman, J. N. 1980, *ApJ*, 236, 577
 Brüns, C., Kerp, J., Staveley-Smith, L., Mebold, U., Putman, M. E., Haynes, R. F., Kalberla, P. M. W., Muller, E., & Filipovic, M. D. 2005, *A&A*, 432, 45
 Cannon, J. M., Skillman, E. D., Sembach, K. R., & Bomans, D. J. 2004, *ApJ*, submitted
 Cen, R., & Ostriker, J. P. 1999, *ApJ*, 514, 1
 Collins, J. A., Benjamin, R. A., & Rand, R. J. 2002, *ApJ*, 578, 98
 Collins, J. A., Shull, J. M., & Giroux, M. L. 2004, *ApJ*, 605, 216
 Collins, J. A., Shull, J. M., & Giroux, M. L. 2005, *ApJ*, 623, 196
 Danforth, C. W., & Shull, J. M. 2005, *ApJ*, 624, 555
 Danforth, C. W., Shull, J. M., Rosenberg, J. L., & Stocke, J. T. 2006, *ApJ*, 640, 716
 Davé, R., et al. 2001, *ApJ*, 552, 473
 Einasto, J., & Lynden-Bell, D. 1982, *MNRAS*, 199, 67
 Esquivel, A., Benjamin, R. A., Cho, J., Lazarian, A., & Leitner, S. N. 2005, *AIPC*, 784, 489
 Fang, T. T., Sembach, K. R., & Canizares, C. R. 2003, *ApJ*, 586, L49
 Fox, A. J., Savage, B. D., Wakker, B. P., Richter, P., Sembach, K. R., & Tripp, T. M. 2004, *ApJ*, 602, 738
 Fox, A. J., Wakker, B. P., Savage, B. D., Sembach, K. R., Tripp, T. M., & Bland-Hawthorn, J. 2005, *ApJ*, 630, 332
 Fox, A. J., Savage, B. D., & Wakker, B. P. 2005, *AJ*, 130, 2418
 Futamoto, K., Mitsuda, K., Takei, Y., Fujimoto, R., & Yamasaki, N. Y. 2004, *ApJ*, 605, 793
 Ganguly, R., Sembach, K. R., Tripp, T. M., & Savage, B. D. 2005, *ApJS*, 157, 251
 Heckman, T. M., Sembach, K. R., Meurer, G. R., Strickland, D. K., Martin, C. L., Calzetti, D., & Leitherer, C. 2001, *ApJ*, 554, 1021
 Houck, J. C., & Bregman, J. N. 1990, *ApJ*, 352, 506
 Howk, J. C., Sembach, K. R., & Savage, B. D. 2003, *ApJ*, 586, 249
 Hulsbosch, A. N. M., & Wakker, B. P. 1988, *A&AS*, 75, 191
 Indebetouw, R., & Shull, J. M. 2004, *ApJ*, 605, 205
 Karachentsev, I. D., & Makarov, D. A. 1996, *AJ*, 111, 794
 Lockman, F. J. 1984, *ApJ*, 283, 90
 Mac Low, M.-M., & Ferrara, A. 1999, *ApJ*, 513, 142
 McKernan, B., Yaqoob, T., & Reynolds, C. S. 2004, *ApJ*, 617, 232
 Moos, H. W., et al. 2000, *ApJ*, 538, L1
 Morton, D. C. 2003, *ApJS*, 149, 205
 Nicastro, N. et al. 2002, *ApJ*, 573, 157
 Nicastro, N. et al. 2003, *Nature*, 421, 719
 Nicastro, N. 2005, *ASP Conf. Ser.* Vol. 216, ed. M. Colless, L. Staveley-Smith, & R. Stathakis, p297
 Oosterloo, T. 2004, in "High-Velocity Clouds", ed. H. van Woerden et al., *ASSL*, Vol 312 (Kluwer), 125
 Pisano, D. J., Barnes, D., Gibson, B., Staveley-Smith, L., Freeman, K. C., & Kilborn, V. A. 2004, *ApJ*, 610, L17
 Richter, P. 2006, preprint ([astro-ph/0602343](http://arxiv.org/abs/astro-ph/0602343))
 Sahnow, D., et al. 2000, *ApJ*, 538, L7
 Savage, B. D., et al. 2003, *ApJS*, 146, 125
 Savage, B. D., Wakker, B. W., Fox, A. J., & Sembach, K. R. 2005, *ApJ*, 619, 863
 Savage, B. D., & Sembach, K. R. 1991, *ApJ*, 379, 245
 Sembach, K. R., & Savage, B. D. 1992, *ApJS*, 83, 147
 Sembach, K. R., Savage, B. D., Lu, L., & Murphy, E. M. 1995, *ApJ*, 451, 616
 Sembach, K. R., & Savage, B. D., Lu, L., & Murphy, E. M. 1999, *ApJ*, 515, 108
 Sembach, K. R., Howk, J. C., Savage, B. D., Shull, J. M., & Oegerle, W. R. 2001, *ApJ*, 561, 573
 Sembach, K. R., et al. 2003, *ApJS*, 146, 165 (S03)
 Shapiro, P. R., & Field, G. B. 1976, *ApJ*, 205, 762
 Spitzer, L. 1978, "Physical Processes in the Interstellar Medium", John Wiley, New York
 Strickland, D. K., & Stevens, I. R. 2000, *MNRAS*, 314, 511
 Sutherland, R. S., & Dopita, M. A. 1993, *ApJS*, 88, 253
 Veilleux, S., Cecil, G., & Bland-Hawthorn, J. 2005, *ARA&A*, 43, 1
 Wakker, B. P., et al. 2003, *ApJS*, 146, 1
 Wakker, B. P. 2006, *ApJS*, in press ([astro-ph/0512444](http://arxiv.org/abs/astro-ph/0512444))
 Wang, Q. D., et al. 2005, *ApJ*, 635, 386
 Williams, R. J., Mathur, S., & Nicastro, F. 2005, *ApJ*, 631, 856
 Williams, R. J., Mathur, S., & Nicastro, F. 2006, *ApJ*, submitted ([astro-ph/0512003](http://arxiv.org/abs/astro-ph/0512003))
 Zsargó, J., Sembach, K. R., Howk, J. C., & Savage, B. D. 2003, *ApJ*, 586, 1019

TABLE 1
 ALL SIGHT LINES SEARCHED FOR HIGH-VELOCITY O VI

| Sight Line | <i>l</i> ($^{\circ}$) | <i>b</i> ($^{\circ}$) | Program ID | CALFUSE | t_{exp}^a (ks) | F_{1030}^b (flux units) | S/N_{1030}^c |
|-------------|----------------------------|----------------------------|--|--|---------------------|------------------------------|----------------|
| MRK279 | 115.04 | 46.86 | P1080303 P1080304 D1540101 | v2.4 v2.4 v2.4 | 183.3 | 10.1 | 44.1 |
| MRK817 | 100.30 | 53.50 | P1080403 P1080404 | v2.1 v2.1 | 187.4 | 9.6 | 41.5 |
| PG1259+593 | 120.60 | 58.10 | P1080101 P1080102 P1080103 P1080104 P1080105 P1080106 P1080107 P1080108 P1080109 | v2.1 v2.1 v2.1 v2.1 v2.1 v2.1 v2.1 v2.1 v2.1 | 162.3 | 1.8 | 37.3 |
| MRK876 | 98.30 | 40.40 | P1073101 D0280203 | v2.1 v2.4 | 132.2 | 6.3 | 33.3 |
| NGC4151 | 155.10 | 75.10 | C0920101 | v2.1 | 96.8 | 7.3 | 32.9 |
| PKS2155-304 | 17.73 | -52.25 | P1080701 P1080703 P1080705 | v2.1 v2.1 v2.1 | 123.2 | 2.8 | 31.7 |
| 3C273.0 | 290.00 | 64.40 | P1013501 | v2.1 | 42.3 | 6.9 | 31.2 |
| PG0804+761 | 138.28 | 31.03 | P1011901 P1011903 S6011001 S6011002 | v2.1 v2.4 v2.1 v2.1 | 174.0 | 7.0 | 30.6 |
| MRK509 | 36.00 | -29.90 | X0170101 X0170102 P1080601 | v2.4 v2.4 v2.1 | 113.0 | 6.7 | 29.5 |
| NGC1068 | 172.10 | -51.93 | P1110202 | v2.1 | 22.6 | 2.3 | 29.3 |
| MRK421 | 179.80 | 65.00 | P1012901 Z0100101 Z0100102 Z0100103 | v2.1 v2.4 v2.4 v2.4 | 83.8 | 9.6 | 29.1 |
| H1821+643 | 94.00 | 27.42 | P1016402 P1016405 C0950201 C0950202 | v2.4 v2.4 v2.4 v2.4 | 280.2 | 3.0 | 27.9 |
| MRK335 | 108.76 | -41.42 | P1010203 P1010204 | v2.4 v2.1 | 97.0 | 7.1 | 27.0 |
| NGC1705 | 261.10 | -38.70 | A0460102 A0460103 | v2.4 v2.4 | 21.3 | 6.8 | 26.7 |
| PG1116+215 | 223.40 | 68.20 | P1013101 P1013102 P1013103 P1013104 P1013105 | v2.1 v2.1 v2.1 v2.1 v2.1 | 76.9 | 5.7 | 25.5 |
| HE0226-4110 | 253.90 | -65.80 | P2071301 P1019101 P1019102 P1019103 P1019104 D0270101 D0270102 D0270103 | v2.1 v2.1 v2.4 v2.4 v2.4 v2.4 v2.4 v2.4 | 207.8 | 2.7 | 24.6 |
| PG0953+414 | 179.80 | 51.70 | P1012201 P1012202 | v2.1 v2.4 | 72.1 | 5.2 | 24.3 |
| MRK1383 | 349.20 | 55.10 | P1014801 P2670101 | v2.1 v2.1 | 64.5 | 6.6 | 23.1 |
| NGC5236 | 314.58 | 31.97 | A0460505 | v2.4 | 26.5 | 4.1 | 20.2 |
| TON S210 | 224.97 | -83.16 | P1070301 P1070302 | v2.1 v2.1 | 54.5 | 6.2 | 20.2 |
| PG0844+349 | 188.60 | 38.00 | P1012002 D0280301 D0280302 D0280303 D0280304 | v2.4 v2.4 v2.4 v2.4 v2.4 | 81.7 | 3.7 | 20.0 |
| PG1211+143 | 267.55 | 74.31 | P1072001 | v2.4 | 52.2 | 5.4 | 19.0 |
| PKS0558-504 | 258.00 | -28.60 | P1011504 C1490601 | v2.4 v2.4 | 93.4 | 3.3 | 18.8 |
| PKS0405-12 | 204.90 | -41.80 | B0870101 D1030101 D1030102 D1030103 | v2.1 v2.4 v2.4 v2.4 | 140.5 | 2.2 | 18.6 |
| MRK290 | 91.49 | 47.95 | P1072901 D0760101 | v2.1 v2.4 | 80.7 | 3.4 | 18.5 |

TABLE 1 — *Continued*

| Sight Line | <i>l</i> ($^{\circ}$) | <i>b</i> ($^{\circ}$) | Program ID | CALFUSE | <i>t_{exp}</i> ^a (ks) | <i>F₁₀₃₀</i> ^b (flux units) | S/N ₁₀₃₀ ^c |
|---------------|----------------------------|----------------------------|--|--|---|--|----------------------------------|
| VIIIZw118 | 151.36 | 25.99 | D0760102 E0840101 P1011604 P1011605 P1011606 S6011301 | v2.4 v2.4 v2.1 v2.4 v2.4 v2.1 | 165.4 | 2.0 | 18.3 |
| NGC3690 | 141.90 | 55.41 | B0040201 B0040202 | v2.1 v2.1 | 59.7 | 5.6 | 17.9 |
| PKS2005-489 | 350.40 | -32.60 | P1073801 C1490301 C1490302 | v2.1 v2.1 v2.1 | 49.2 | 5.0 | 17.5 |
| PG1011-040 | 246.50 | 40.75 | B0790101 | v2.4 | 86.3 | 2.6 | 17.2 |
| PHL1811 | 47.47 | -44.82 | P2071101 P1081001 P1081002 P1081003 | v2.4 v2.4 v2.4 v2.4 | 47.7 | 4.9 | 17.1 |
| NGC4670 | 212.70 | 88.60 | B0220301 B0220302 B0220303 | v2.1 v2.1 v2.1 | 35.4 | 0.8 | 16.7 |
| MRK1513 | 63.67 | -29.07 | P1018301 P1018302 P1018303 | v2.4 v2.4 v2.4 | 42.9 | 3.9 | 16.3 |
| NGC7469 | 83.10 | -45.47 | P1018703 | v2.4 | 42.9 | 5.9 | 16.0 |
| ESO141-G55 | 338.20 | -26.70 | I9040104 | v2.4 | 40.4 | 5.2 | 16.0 |
| MRK205 | 125.45 | 41.67 | Q1060203 S6010801 D0540101 D0540102 D0540103 | v2.4 v2.1 v2.4 v2.4 v2.4 | 206.3 | 1.3 | 15.9 |
| PG1302-102 | 308.60 | 52.20 | P1080201 P1080202 P1080203 | v2.1 v2.1 v2.1 | 144.9 | 1.6 | 15.7 |
| MRK153 | 156.73 | 56.01 | A0940101 | v2.4 | 65.1 | 7.8 | 15.2 |
| MS0700.7+6338 | 152.50 | 25.60 | P2072701 S6011501 D0550501 | v2.4 v2.4 v2.4 | 106.4 | 1.9 | 14.6 |
| PG1626+554 | 84.51 | 42.19 | C0370101 | v2.1 | 91.2 | 1.5 | 14.1 |
| MRK59 | 111.54 | 82.11 | A0360202 | v2.4 | 9.8 | 2.2 | 13.9 |
| 3C249.1 | 130.39 | 38.55 | P1071601 P1071602 S6010901 P1071603 D1170101 D1170102 D1170103 | v2.1 v2.1 v2.1 v2.4 v2.4 v2.4 v2.4 | 219.4 | 1.1 | 13.8 |
| TON S180 | 139.00 | -85.10 | P1010502 D0280101 | v2.4 v2.4 | 28.6 | 6.3 | 13.6 |
| NGC7714 | 88.22 | -55.56 | A0230404 A0860606 B0040301 C0370206 C0370201 C0370202 C0370203 C0370204 C0370205 | v2.1 v2.1 v2.1 v2.4 v2.0 v2.0 v2.0 v2.0 v2.0 | 131.6 | 2.5 | 12.8 |
| NGC1741 | 203.72 | -26.29 | C0480201 C0480202 | v2.4 v2.4 | 29.3 | 5.2 | 12.7 |
| MRK9 | 158.36 | 28.75 | P1071101 P1071102 P1071103 S6011601 | v2.4 v2.4 v2.4 v2.1 | 61.5 | 2.3 | 12.6 |
| MRK106 | 161.14 | 42.88 | C1490501 | v2.4 | 121.9 | 1.6 | 12.1 |
| MRK586 | 157.60 | -54.93 | D0550101 D0550102 | v2.4 v2.4 | 64.0 | 2.1 | 11.9 |
| PG1553+113 | 21.91 | 43.96 | E5260501 E5260502 E5260503 | v2.4 v2.4 v2.4 | 50.7 | 2.7 | 11.9 |
| 1H0717+714 | 144.00 | 28.00 | Z9071301 | v2.4 | 55.6 | 2.7 | 11.7 |
| 1H0707-495 | 260.20 | -17.70 | B1050101 B1050102 B1050103 | v2.4 v2.4 v2.4 | 67.0 | 1.8 | 11.7 |
| MRC2251-178 | 46.15 | -61.32 | P1111010 | v2.1 | 52.5 | 2.2 | 11.6 |
| ESO572-G34 | 286.10 | 42.10 | B0220201 | v2.1 | 25.5 | 6.4 | 11.2 |
| HS0624+6907 | 145.71 | 23.35 | P1071001 | v2.1 | 116.0 | 1.0 | 11.0 |

TABLE 1 — *Continued*

| Sight Line | <i>l</i> ($^{\circ}$) | <i>b</i> ($^{\circ}$) | Program ID | CALFUSE | <i>t_{exp}</i> ^a (ks) | <i>F₁₀₃₀</i> ^b (flux units) | S/N ₁₀₃₀ ^c |
|------------|----------------------------|----------------------------|----------------|----------|---|--|----------------------------------|
| MRK1095 | 201.70 | -21.13 | P1071002 | v2.1 | | | |
| | | | S6011201 | v2.1 | | | |
| | | | S6011202 | v2.1 | | | |
| | | | P1011201 | v2.1 | 56.3 | 2.0 | 11.0 |
| NGC625 | 273.70 | -73.10 | P1011202 | v2.1 | | | |
| | | | P1011203 | v2.1 | | | |
| | | | D0400101 | v2.4 | 56.7 | 2.7 | 11.0 |
| | | | IRAS08339+6517 | B0040101 | v2.4 | 0.0 | 2.4 |
| NGC985 | 180.84 | -59.49 | B0040102 | v2.4 | | | |
| | | | P1010903 | v2.4 | 68.0 | 3.3 | 10.7 |
| | | | MRK477 | D1180101 | v2.4 | 157.7 | 1.0 |
| | | | MRK501 | P1073301 | v2.1 | 30.0 | 3.1 |
| NGC1399 | 93.04 | 56.82 | C0810101 | v2.4 | | | |
| | | | NGC1399 | 236.72 | -53.63 | A0880303 | v2.4 |
| | | | | | | A0880304 | v2.4 |
| | | | NGC1522 | 262.00 | -45.97 | Z9090501 | v2.4 |
| MRK829 | 58.76 | 63.25 | MRK829 | 59.20 | 65.00 | A0220401 | v2.1 |
| | | | MRK478 | 59.20 | 65.00 | P1110101 | v2.4 |
| | | | HE1143-1810 | 281.90 | 41.70 | P1071901 | v2.1 |
| | | | ESO265-G23 | 285.91 | 16.59 | A1210405 | v2.1 |
| NGC5408 | 285.91 | 16.59 | | | | A1210407 | v2.1 |
| | | | | | | A1210408 | v2.1 |
| | | | | | | A1210409 | v2.1 |
| | | | NGC5408 | 317.15 | 19.50 | Z9090901 | v2.4 |

^a Combined exposure time.^b Flux at 1030 Å; 1 flux unit = 10^{-14} erg cm $^{-2}$ s $^{-1}$ Å $^{-1}$.^c S/N per resolution element at 1030 Å in combined spectrum.

TABLE 2
 DETECTIONS OF HIGHLY IONIZED HVCs

| Sight Line | $v_{min,max}^a$ | O VI | | | | C III | | | | H I | | | | |
|--|-----------------|---------------|------------|--------------------------|-------------------|--------------|------------|--------------------------|-------------------|-------------------|--------------|------------|-----------------------|-------------------|
| | | \bar{v}^b | b^c | $\log N_a^d$ | Sig. ^e | \bar{v}^b | b^c | $\log N_a^d$ | Sig. ^e | Line ^f | \bar{v}^b | b^c | $\log N_a^d$ | Sig. ^e |
| Sight lines with high-negative-velocity O VI absorption | | | | | | | | | | | | | | |
| PKS2155-304 | -300, -200 | -244 \pm 6 | 36 \pm 6 | 13.51 $^{+0.09}_{-0.11}$ | 12.6 | -271 \pm 4 | 30 \pm 4 | 13.49 $^{+0.04}_{-0.05}$ | 18.8 | 926 | -253 \pm 2 | 18 \pm 6 | 15.5 $^{+0.3}_{-0.3}$ | 10.3 |
| | -200, -70 | -127 \pm 5 | 47 \pm 2 | 13.90 $^{+0.05}_{-0.05}$ | 26.6 | -159 \pm 3 | 44 \pm 2 | 13.91 $^{+0.03}_{-0.03}$ | 41.6 | 926 | -126 \pm 5 | 32 \pm 6 | 16.1 $^{+0.3}_{-0.3}$ | 28.9 |
| MRK335 | -375, -250 | -302 \pm 5 | 45 \pm 2 | 13.95 $^{+0.05}_{-0.05}$ | 18.8 | -320 \pm 4 | 40 \pm 2 | 14.04 $^{+0.06}_{-0.07}$ | 38.2 | 926 | ... | ... | >16.4 | ... |
| | -180, -80 | -137 \pm 10 | 41 \pm 2 | 13.74 $^{+0.07}_{-0.08}$ | 14.0 | ... | ... | >14.24 | ... | 926 | ... | ... | >16.2 | ... |
| TON S210 | -270, -125 | -187 \pm 9 | 57 \pm 5 | 13.86 $^{+0.08}_{-0.09}$ | 9.6 | ... | ... | >14.27 | ... | 926 | ... | ... | >16.8 | ... |
| PHL1811 | -365, -250 | -311 \pm 8 | 42 \pm 5 | 13.79 $^{+0.09}_{-0.12}$ | 5.8 | ... | ... | ... | g | ... | ... | ... | ... | g |
| | -190, -80 | -140 \pm 4 | 33 \pm 3 | 14.31 $^{+0.03}_{-0.04}$ | 17.5 | ... | ... | ... | g | ... | ... | ... | ... | g |
| MRK1513 | -390, -220 | -301 \pm 1 | 51 \pm 1 | 14.46 $^{+0.03}_{-0.04}$ | 22.8 | ... | ... | >13.96 | ... | 949 | ... | ... | >15.8 | ... |
| NGC7469 | -380, -250 | -308 \pm 6 | 50 \pm 5 | 14.13 $^{+0.05}_{-0.06}$ | 14.0 | ... | ... | ... | g | ... | ... | ... | ... | g |
| | -200, -100 | -169 \pm 5 | 31 \pm 2 | 14.04 $^{+0.06}_{-0.07}$ | 12.8 | ... | ... | ... | g | ... | ... | ... | ... | g |
| NGC7714 | -310, -220 | -262 \pm 2 | 31 \pm 1 | 14.16 $^{+0.05}_{-0.06}$ | 12.0 | ... | ... | >14.00 | ... | 937 | ... | ... | >16.0 | ... |
| | -200, -100 | -149 \pm 5 | 33 \pm 4 | 13.66 $^{+0.13}_{-0.20}$ | 3.7 | ... | ... | >13.84 | ... | 937 | ... | ... | >15.9 | ... |
| Sight lines with high-positive-velocity O VI absorption | | | | | | | | | | | | | | |
| MRK817 | 50, 110 | 71 \pm 9 | 21 \pm 6 | 13.04 $^{+0.20}_{-0.40}$ | 7.3 | 75 \pm 9 | 18 \pm 3 | 12.77 $^{+0.11}_{-0.15}$ | 7.2 | 926 | 72 \pm 6 | 14 \pm 6 | 15.2 $^{+0.3}_{-0.3}$ | 7.5 |
| | 140, 220 | 189 \pm 5 | 21 \pm 4 | 13.03 $^{+0.21}_{-0.41}$ | 6.1 | ... | ... | <12.54 | ... | 926 | ... | ... | <15.1 | ... |
| NGC4151 | 120, 240 | 170 \pm 5 | 37 \pm 4 | 13.96 $^{+0.06}_{-0.07}$ | 6.8 | 155 \pm 3 | 30 \pm 3 | 13.68 $^{+0.04}_{-0.05}$ | 17.1 | 972 | 158 \pm 3 | 25 \pm 6 | 15.2 $^{+0.3}_{-0.3}$ | 34.2 |
| 3C273.0 | 170, 250 | 206 \pm 4 | 30 \pm 2 | 13.44 $^{+0.10}_{-0.13}$ | 12.8 | ... | ... | ... | g | ... | 926 | ... | ... | <15.0 |
| MRK421 | 65, 160 | 94 \pm 8 | 30 \pm 7 | 13.48 $^{+0.08}_{-0.10}$ | 8.2 | ... | ... | <12.84 | ... | 949 | ... | ... | <14.7 | ... |
| NGC1705 | 200, 400 | 300 \pm 4 | 62 \pm 4 | 14.33 $^{+0.03}_{-0.03}$ | 27.4 | ... | ... | >14.40 | ... | 926 | ... | ... | >16.8 | ... |
| PG1116+215 | 105, 305 | 173 \pm 4 | 42 \pm 7 | 14.02 $^{+0.07}_{-0.08}$ | 5.9 | ... | ... | >14.14 | ... | 923 | ... | ... | >16.7 | ... |
| HE0226-4110 | 100, 230 | 164 \pm 4 | 42 \pm 3 | 13.82 $^{+0.06}_{-0.07}$ | 11.4 | ... | ... | >14.14 | ... | 920 | ... | ... | >16.9 | ... |
| PG0953+414 | 100, 225 | 137 \pm 14 | 47 \pm 7 | 13.49 $^{+0.15}_{-0.22}$ | 4.7 | 134 \pm 5 | 31 \pm 2 | 13.66 $^{+0.05}_{-0.06}$ | 14.3 | 923 | 122 \pm 6 | 21 \pm 6 | 16.1 $^{+0.3}_{-0.3}$ | 12.6 |
| MRK1383 | 100, 160 | 133 \pm 6 | 21 \pm 3 | 13.14 $^{+0.19}_{-0.34}$ | 3.9 | 116 \pm 12 | 24 \pm 4 | 13.14 $^{+0.11}_{-0.15}$ | 5.3 | 937 | ... | ... | <15.0 | ... |
| PG0844+349 | 110, 230 | 148 \pm 8 | 45 \pm 4 | 13.63 $^{+0.10}_{-0.14}$ | 5.4 | 137 \pm 9 | 33 \pm 5 | 13.68 $^{+0.07}_{-0.08}$ | 11.2 | 926 | 128 \pm 9 | 25 \pm 6 | 15.8 $^{+0.3}_{-0.3}$ | 7.3 |
| PG1211+143 | 130, 220 | 173 \pm 9 | 35 \pm 3 | 13.34 $^{+0.18}_{-0.31}$ | 3.3 | 181 \pm 3 | 22 \pm 4 | 13.23 $^{+0.08}_{-0.10}$ | 7.1 | 930 | 175 \pm 2 | 23 \pm 6 | 15.7 $^{+0.3}_{-0.3}$ | 10.5 |
| PKS0558-504 | 210, 315 | 258 \pm 2 | 39 \pm 2 | 13.76 $^{+0.09}_{-0.11}$ | 8.0 | 260 \pm 20 | 27 \pm 3 | 13.67 $^{+0.16}_{-0.26}$ | 8.1 | 926 | ... | ... | >16.2 | ... |
| PKS0405-12 | 110, 205 | 153 \pm 6 | 36 \pm 2 | 13.54 $^{+0.12}_{-0.18}$ | 5.4 | 139 \pm 6 | 41 \pm 5 | 13.35 $^{+0.13}_{-0.18}$ | 3.9 | 949 | 136 \pm 2 | 17 \pm 6 | 15.2 $^{+0.3}_{-0.3}$ | 5.5 |
| PKS2005-489 | 115, 220 | 143 \pm 8 | 30 \pm 4 | 13.71 $^{+0.10}_{-0.13}$ | 6.7 | ... | ... | >13.69 | ... | 926 | 166 \pm 5 | 26 \pm 6 | 16.1 $^{+0.3}_{-0.3}$ | 14.5 |
| PG1011-040 | 100, 240 | 144 \pm 7 | 46 \pm 3 | 14.18 $^{+0.05}_{-0.06}$ | 14.2 | ... | ... | >14.06 | ... | 949 | ... | ... | >16.1 | ... |
| | 240, 320 | 279 \pm 20 | 29 \pm 2 | 13.53 $^{+0.13}_{-0.18}$ | 4.8 | ... | ... | <13.07 | ... | 949 | 263 \pm 9 | 21 \pm 6 | 15.1 $^{+0.3}_{-0.3}$ | 6.5 |
| NGC4670 | 320, 380 | 353 \pm 3 | 21 \pm 3 | 13.92 $^{+0.05}_{-0.06}$ | 12.8 | 347 \pm 3 | 21 \pm 3 | 13.34 $^{+0.09}_{-0.11}$ | 7.0 | 972 | 344 \pm 3 | 23 \pm 6 | 15.0 $^{+0.3}_{-0.3}$ | 4.6 |
| ESO141-G55 | 135, 210 | 174 \pm 4 | 25 \pm 4 | 13.35 $^{+0.17}_{-0.28}$ | 3.3 | 173 \pm 7 | 33 \pm 3 | 13.03 $^{+0.15}_{-0.22}$ | 3.6 | 926 | ... | ... | <15.2 | ... |
| PG1302-102 | 190, 340 | 255 \pm 3 | 51 \pm 3 | 14.01 $^{+0.07}_{-0.09}$ | 9.6 | ... | ... | <13.60 | ... | 930 | ... | ... | <15.8 | ... |
| MS0700.7+6338 | 90, 180 | 134 \pm 3 | 29 \pm 2 | 13.68 $^{+0.11}_{-0.15}$ | 5.0 | ... | ... | <13.49 | ... | 949 | ... | ... | <15.5 | ... |
| 1H0707-495 | 95, 195 | 143 \pm 3 | 28 \pm 3 | 13.68 $^{+0.14}_{-0.22}$ | 3.9 | ... | ... | >13.70 | ... | 926 | ... | ... | >16.4 | ... |
| ESO572-G34 | 100, 275 | 166 \pm 6 | 61 \pm 4 | 14.42 $^{+0.04}_{-0.05}$ | 15.3 | ... | ... | >14.16 | ... | 930 | ... | ... | >16.6 | ... |
| NGC625 | 115, 225 | 157 \pm 6 | 36 \pm 5 | 14.05 $^{+0.09}_{-0.11}$ | 6.3 | ... | ... | ... | g | ... | ... | ... | ... | g |
| HE1143-1810 | 100, 200 | 140 \pm 7 | 40 \pm 2 | 14.20 $^{+0.08}_{-0.09}$ | 9.6 | ... | ... | >14.21 | ... | 937 | ... | ... | >16.5 | ... |
| | 200, 300 | 246 \pm 7 | 32 \pm 4 | 13.80 $^{+0.15}_{-0.23}$ | 3.7 | ... | ... | <13.37 | ... | 937 | ... | ... | <15.5 | ... |
| Sight lines with high-negative- and high-positive-velocity O VI absorption | | | | | | | | | | | | | | |
| MRK509 | -350, -200 | -260 \pm 3 | 45 \pm 3 | 14.15 $^{+0.03}_{-0.03}$ | 27.1 | ... | ... | >14.39 | ... | 926 | ... | ... | >16.7 | ... |
| | -200, -100 | -151 \pm 7 | 42 \pm 2 | 13.80 $^{+0.06}_{-0.07}$ | 15.5 | ... | ... | >13.84 | ... | 926 | ... | ... | >16.0 | ... |

TABLE 2 — *Continued*

| Sight Line | $v_{min,max}^a$ | O VI | | | | C III | | | | H I | | | | | |
|------------|-----------------|-------------|-------|-------------------------|-------------------|-------------|-------|-------------------------|-------------------|-------------------|-------------|-------|--------------|-------------------|-----|
| | | \bar{v}^b | b^c | $\log N_a^d$ | Sig. ^e | \bar{v}^b | b^c | $\log N_a^d$ | Sig. ^e | Line ^f | \bar{v}^b | b^c | $\log N_a^d$ | Sig. ^e | |
| TON S180 | 100, 175 | 123±10 | 28±3 | $13.61^{+0.08}_{-0.10}$ | 11.1 | 114±6 | 24±2 | $13.72^{+0.06}_{-0.06}$ | 18.0 | 926 | ... | ... | >16.1 | ... | |
| | -200, -100 | -151±4 | 34±2 | $14.20^{+0.05}_{-0.05}$ | 15.9 | ... | ... | >14.22 | ... | 972 | ... | ... | >15.8 | ... | |
| | 215, 290 | 251±2 | 22±3 | $13.66^{+0.11}_{-0.15}$ | 5.4 | ... | ... | <13.31 | ... | 972 | ... | ... | <14.7 | ... | |
| NGC1522 | -250, -100 | -178±4 | 54±3 | $13.86^{+0.15}_{-0.22}$ | 3.2 | ... | ... | ... | g | ... | ... | ... | ... | g | ... |
| | 205, 360 | 284±3 | 51±3 | $14.15^{+0.07}_{-0.09}$ | 7.6 | ... | ... | ... | g | ... | ... | ... | ... | g | ... |
| NGC5408 | -200, -100 | -151±5 | 38±3 | $13.96^{+0.12}_{-0.16}$ | 4.8 | ... | ... | ... | g | ... | ... | ... | ... | g | ... |
| | 100, 250 | 148±8 | 51±3 | $14.50^{+0.06}_{-0.07}$ | 11.4 | ... | ... | ... | g | ... | ... | ... | ... | g | ... |

^a v_{min} and v_{max} are the observed minimum and maximum velocity of high-velocity O VI absorption.

^b Velocity centroid of high-velocity absorption, obtained from $\bar{v} = \int_{v_{min}}^{v_{max}} v \tau_a(v) dv / \int_{v_{min}}^{v_{max}} \tau_a(v) dv$.

^c Doppler parameter (width) of high-velocity absorption, obtained from $b = \sqrt{2 \int_{v_{min}}^{v_{max}} (v - \bar{v})^2 \tau_a(v) dv / \int_{v_{min}}^{v_{max}} \tau_a(v) dv}$.

^d Column densities calculated using the apparent optical depth (AOD) technique, including statistical, continuum placement, and systematic errors.

^e Detection significance, $W_\lambda / \sigma(W_\lambda)$.

^f H I Lyman series line used in measurement.

^g No measurement possible, due to blending or insufficient flux in SiC channels.

TABLE 3
 3 σ NON-DETECTIONS OF HIGHLY IONIZED HVCs

| Sight Line | -200 to -100 km s ⁻¹ | | 100 to 200 km s ⁻¹ | |
|---------------------------|---------------------------------|---|-------------------------------|---|
| | W_{λ} (mÅ) | log $N(\text{O VI})$ (N in cm ⁻²) | W_{λ} (mÅ) | log $N(\text{O VI})$ (N in cm ⁻²) |
| PG1553+113 | < 80 | <13.81 | < 21 | <13.24 |
| MRC2251-178 | < 67 | <13.73 | < 46 | <13.57 |
| MRK829 | <119 | <13.98 | <100 | <13.91 |
| MRK478 | <122 | <13.99 | < 59 | <13.68 |
| MRK477 | <102 | <13.92 | < 97 | <13.89 |
| MRK59 | < 51 | <13.61 | < 36 | <13.46 |
| 1H0717+714 | < 82 | <13.82 | < 46 | <13.57 |
| VIIIZw118 | < 37 | <13.48 | < 38 | <13.49 |
| MRK153 | < 14 | <13.07 | < 68 | <13.74 |
| MRK586 | < 67 | <13.73 | < 20 | <13.21 |
| MRK9 | < 43 | <13.54 | < 56 | <13.66 |
| MRK106 | < 71 | <13.76 | < 37 | <13.48 |
| NGC1068 | < 36 | <13.47 | < 12 | <12.99 |
| NGC985 | < 72 | <13.76 | < 32 | <13.41 |
| MRK1095 | < 50 | <13.60 | < 5 | <12.62 |
| NGC1741 | < 67 | <13.73 | < 57 | <13.66 |
| NGC1399 | <157 | <14.10 | < 19 | <13.20 |
| PKS2155-304 | ... | ... | <21 | <13.23 |
| TON S210 | ... | ... | <32 | <13.42 |
| PHL1811 | ... | ... | <58 | <13.67 |
| MRK1513 | ... | ... | <34 | <13.44 |
| NGC7469 | ... | ... | <24 | <13.30 |
| NGC7714 | ... | ... | <43 | <13.54 |
| NGC4151 | <18 | <13.18 | ... | ... |
| 3C273.0 | <30 | <13.38 | ... | ... |
| MRK421 | <27 | <13.34 | ... | ... |
| NGC1705 | <14 | <13.07 | ... | ... |
| PG1116+215 | <18 | <13.17 | ... | ... |
| HE0226-4110 | <12 | <13.00 | ... | ... |
| PG0953+414 | <49 | <13.60 | ... | ... |
| MRK1383 | <23 | <13.27 | ... | ... |
| PG0844+349 | <37 | <13.47 | ... | ... |
| PG1211+143 | <51 | <13.61 | ... | ... |
| PKS0558-504 | <44 | <13.55 | ... | ... |
| PKS0405-12 | <26 | <13.33 | ... | ... |
| PKS2005-489 | <52 | <13.63 | ... | ... |
| PG1011-040 | <32 | <13.41 | ... | ... |
| NGC4670 | <23 | <13.28 | ... | ... |
| ESO141-G55 | <51 | <13.61 | ... | ... |
| PG1302-102 | <46 | <13.57 | ... | ... |
| MS0700.7+6338 | <48 | <13.59 | ... | ... |
| 1H0707-495 | <33 | <13.43 | ... | ... |
| ESO572-G34 | <98 | <13.89 | ... | ... |
| NGC625 | <78 | <13.80 | ... | ... |
| HE1143-1810 | <77 | <13.79 | ... | ... |
| MRK501 (ComplexC) | ... | ... | <63 | <13.70 |
| PG1626+554 (ComplexC) | ... | ... | <45 | <13.56 |
| MRK290 (ComplexC) | ... | ... | <41 | <13.52 |
| H1821+643 (OuterArm) | ... | ... | <10 | <12.94 |
| MRK876 (ComplexC) | ... | ... | <23 | <13.27 |
| MRK279 (ComplexC) | ... | ... | <12 | <13.01 |
| PG1259+593 (ComplexC) | ... | ... | <24 | <13.29 |
| MRK205 (ComplexC) | ... | ... | <38 | <13.49 |
| 3C249.1 (nearComplexC) | ... | ... | <35 | <13.46 |
| PG0804+761 (nearComplexA) | ... | ... | <10 | <12.93 |
| NGC3690 (nearComplexC) | ... | ... | <14 | <13.05 |
| HS0624+6907 (OuterArm) | ... | ... | <62 | <13.70 |
| IRAS08339+6517 (ComplexA) | ... | ... | <74 | <13.78 |
| ESO265-G23 (MagStream) | <71 | <13.76 | ... | ... |
| NGC5236 (MagStream) | <80 | <13.81 | ... | ... |

^a See Table 2 for detections in this velocity range.^b Velocity range excluded due to the presence of a 21 cm emitting H I HVC, named in parentheses after the target name.

TABLE 4
ANALYSIS OF HIGHLY IONIZED HVCs

| | (1) $b < 0^\circ$ | (2) $b > 0^\circ$ | (3) $l < 180^\circ$ | (4) $l > 180^\circ$ | (5) With C III | (6) With H I | (7) Wings |
|---------------------------------|----------------------|----------------------|------------------------|------------------------|-------------------|-----------------|--------------|
| All Absorbers | 57% (27/47) | 43% (20/47) | 47% (22/47) | 53% (25/47) | 81% (30/37) | 76% (29/38) | 23% (11/47) |
| With C III | 63% (19/30) | 37% (11/30) | 47% (14/30) | 53% (16/30) | ... | 93% (28/30) | 27% (8/30) |
| With H I | 62% (18/29) | 38% (11/29) | 48% (14/29) | 52% (15/29) | 97% (28/29) | ... | 28% (8/29) |
| Wings | 27% (3/11) | 73% (8/11) | 36% (4/11) | 64% (7/11) | 89% (8/9) | 89% (8/9) | ... |
| $v_{LSR} < 0 \text{ km s}^{-1}$ | 94% (16/17) | 6% (1/17) | 82% (14/17) | 18% (3/17) | 65% (11/17) | 65% (11/17) | 0% (0/17) |
| $v_{LSR} > 0 \text{ km s}^{-1}$ | 37% (11/30) | 63% (19/30) | 27% (8/30) | 73% (22/30) | 63% (19/30) | 60% (18/30) | 37% (11/30) |

NOTE. — Each row refers to a sub-category of the highly ionized HVCs in this study; the table entries in each column represent the percentage of cases in that sub-category falling in different parts of the sky (columns 1 to 4), showing accompanying C III absorption (column 5), showing accompanying H I absorption (column 6), or appearing in the form of wings (column 7).

TABLE 5
PROPERTIES OF WINGS VS COMPONENTS^a

| Category | Num. | $\langle \log N(\text{O VI}) \rangle$ (N in cm^{-2}) | $\langle v_0(\text{O VI}) \rangle$ (km s^{-1}) | $\langle b(\text{O VI}) \rangle$ (km s^{-1}) | With C III | $\left\langle \frac{N_a(\text{C III})}{N_a(\text{O VI})} \right\rangle^b$ | With H I | $\left\langle \frac{N_a(\text{H I})}{N_a(\text{O VI})} \right\rangle^b$ |
|---------------|------|--|--|--|------------|---|----------|---|
| Wings | 11 | 13.85 ± 0.45 | 133 ± 28 | 39 ± 11 | 88% | 1.1 ± 0.4 | 88% | 260 ± 140 |
| PV Components | 19 | 13.69 ± 0.34 | 212 ± 63 | 34 ± 11 | 64% | 0.6 ± 0.2 | 55% | 70 ± 100 |
| NV Components | 17 | 13.97 ± 0.24 | -207 ± 69 | 41 ± 8 | 100% | 1.1 ± 0.1 | 100% | 130 ± 50 |

^a Errors quoted on average quantities represent standard deviation of sample.

^b Only detections are included in this calculation. Cases with upper/lower limits on $N(\text{C III})$ and $N(\text{H I})$ are ignored.

TABLE 6
IONIC RATIOS AND CIE TEMPERATURES^a

| Target | Type ^b | $N_a(\text{C III})/N_a(\text{O VI})$ | T_{CIE} |
|---------------|-------------------|--------------------------------------|-----------|
| PKS2155-304 | NVC | 1.0 ± 0.2 | 5.23 |
| | NVC | 1.0 ± 0.1 | 5.23 |
| MRK335 | NVC | 1.2 ± 0.2 | 5.22 |
| | NVC | >3.2 | <5.21 |
| TON S210 | NVC | >2.6 | <5.21 |
| MRK1513 | NVC | >0.3 | <5.25 |
| NGC7714 | NVC | >0.7 | <5.23 |
| | NVC | >1.5 | <5.22 |
| MRK817 | PVW | 0.5 ± 0.4 | 5.24 |
| | PVC | <0.3 | >5.25 |
| NGC4151 | PVC | 0.5 ± 0.1 | 5.24 |
| MRK421 | PVW | <0.2 | >5.25 |
| NGC1705 | PVC | >1.2 | <5.22 |
| PG1116+215 | PVC | >1.3 | <5.22 |
| HE0226-4110 | PVC | >2.1 | <5.22 |
| PG0953+414 | PVW | 1.5 ± 0.6 | 5.22 |
| MRK1383 | PVC | 1.0 ± 0.6 | 5.23 |
| PG0844+349 | PVW | 1.1 ± 0.4 | 5.23 |
| PG1211+143 | PVC | 0.8 ± 0.4 | 5.23 |
| PKS0558-504 | PVC | 0.8 ± 0.4 | 5.23 |
| PKS0405-12 | PVC | 0.6 ± 0.3 | 5.24 |
| PKS2005-489 | PVW | >1.0 | <5.23 |
| PG1011-040 | PVW | >0.8 | <5.23 |
| | PVC | <0.3 | >5.25 |
| NGC4670 | PVC | 0.3 ± 0.1 | 5.25 |
| ESO141-G55 | PVC | 0.5 ± 0.3 | 5.24 |
| PG1302-102 | PVC | <0.4 | >5.24 |
| MS0700.7+6338 | PVC | <0.6 | >5.24 |
| 1H0707-495 | PVC | >1.0 | <5.23 |
| ESO572-G34 | PVW | >0.5 | <5.24 |
| NGC625 | PVW | <0.6 | >5.24 |
| HE1143-1810 | PVW | >1.0 | <5.23 |
| | PVC | <0.4 | >5.24 |
| MRK509 | NVC | >1.7 | <5.22 |
| | NVC | >1.1 | <5.23 |
| MRK509 | PVW | 1.3 ± 0.3 | 5.22 |
| TON S180 | NVC | >1.0 | <5.23 |
| | PVC | <0.4 | >5.24 |

^a Gas temperatures assume collisional ionization equilibrium and solar carbon and oxygen abundances.

^b Type: PVC=positive-velocity component, PVW=positive-velocity wing, NVC=negative-velocity component. Multiple components in a given sight line are presented in order of increasing velocity.

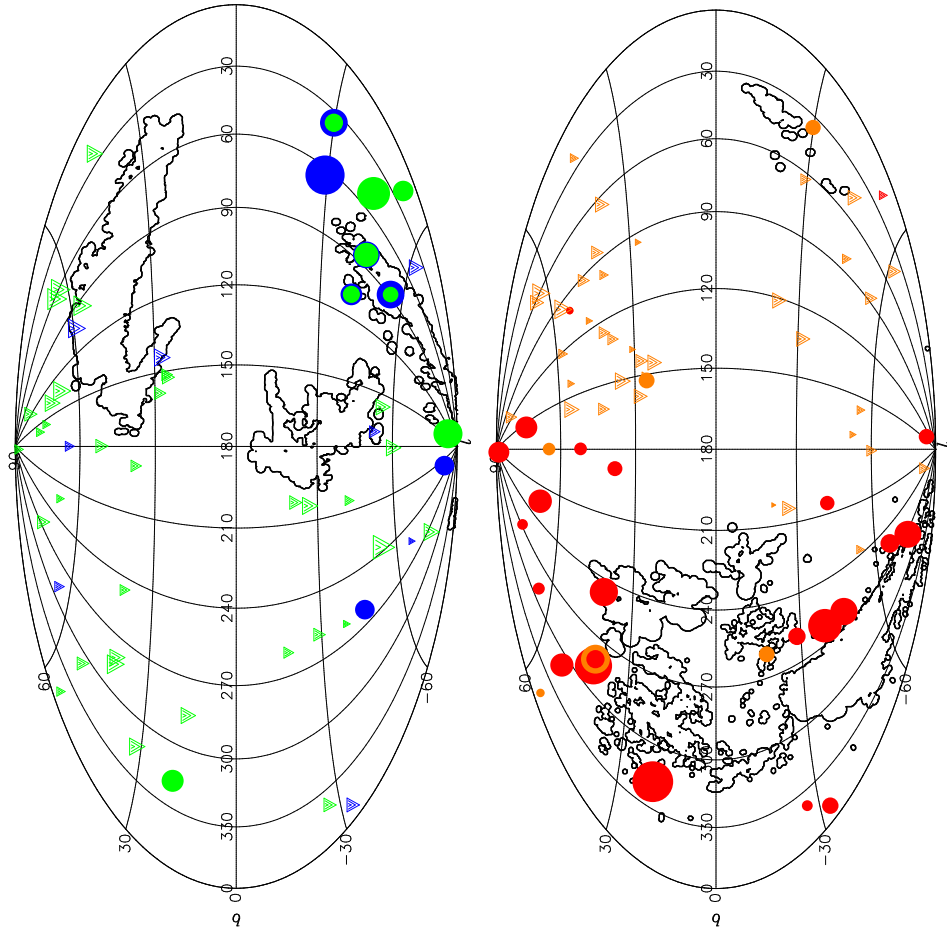


FIG. 1.— Distribution of negative (left) and positive (right) highly ionized HVCs on the sky, using Aitoff projections centered at $l = 180^\circ$, with contours showing H I 21 cm-emitting structures (Complexes A and C, the anti-center clouds, and the Magellanic Stream; Hulsbosch & Wakker 1988). Circles represent detections, coded by central velocity (blue: $-400 < v < -150 \text{ km s}^{-1}$; green: $-150 < v < -100 \text{ km s}^{-1}$; orange: $100 < v < 150 \text{ km s}^{-1}$; red: $150 < v < 400 \text{ km s}^{-1}$) and triangles show non-detections. Symbol sizes are proportional to the column density in the O VI absorber (or to the upper limit for non-detections).

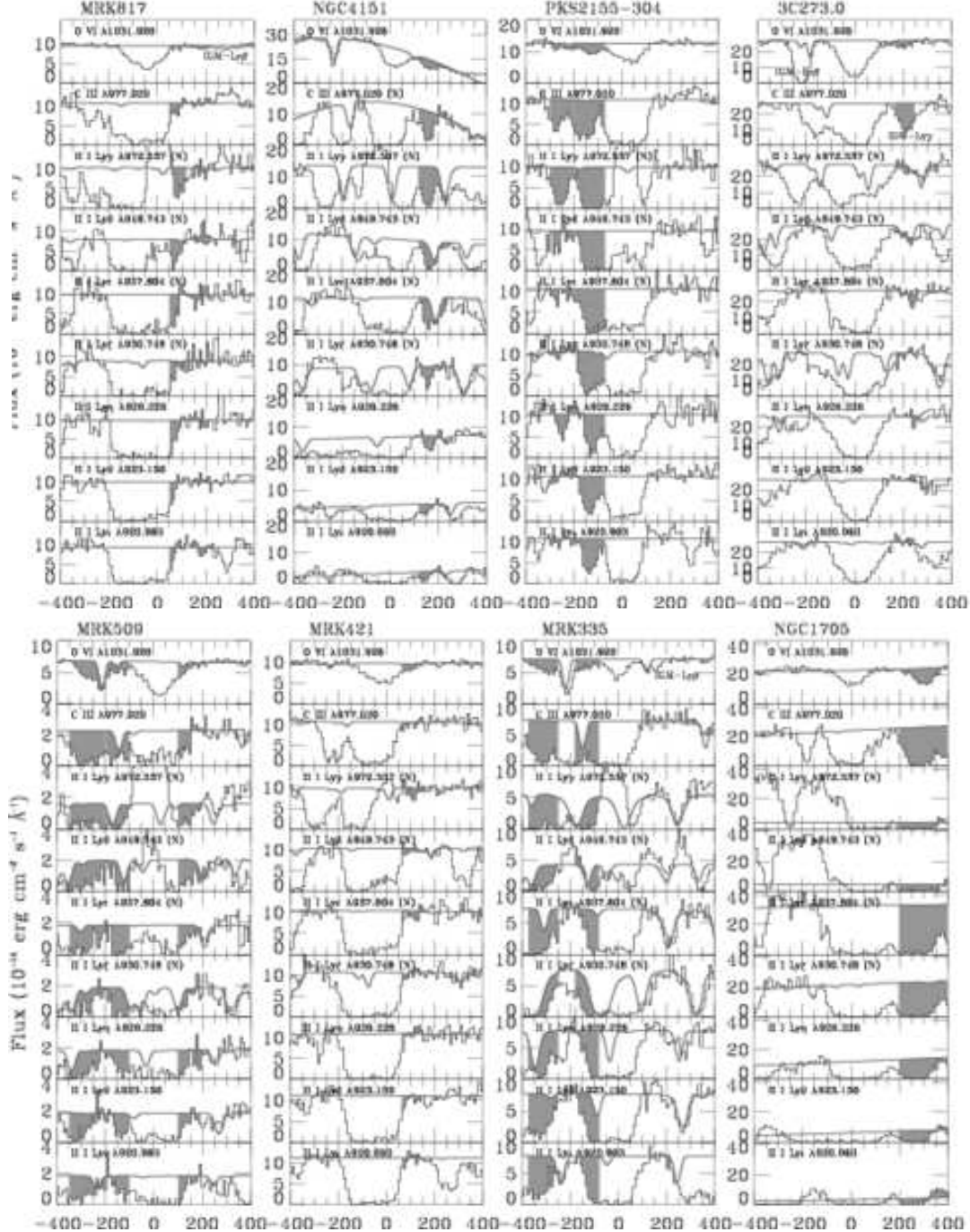


FIG. 2.— O VI, C III, and H I spectra for all highly ionized HVCs, presented in order of decreasing S/N. Gray shading denotes velocity ranges where high-velocity absorption is seen. The continuum placement, including a model for H₂ model, is shown as a gray solid line in each panel.

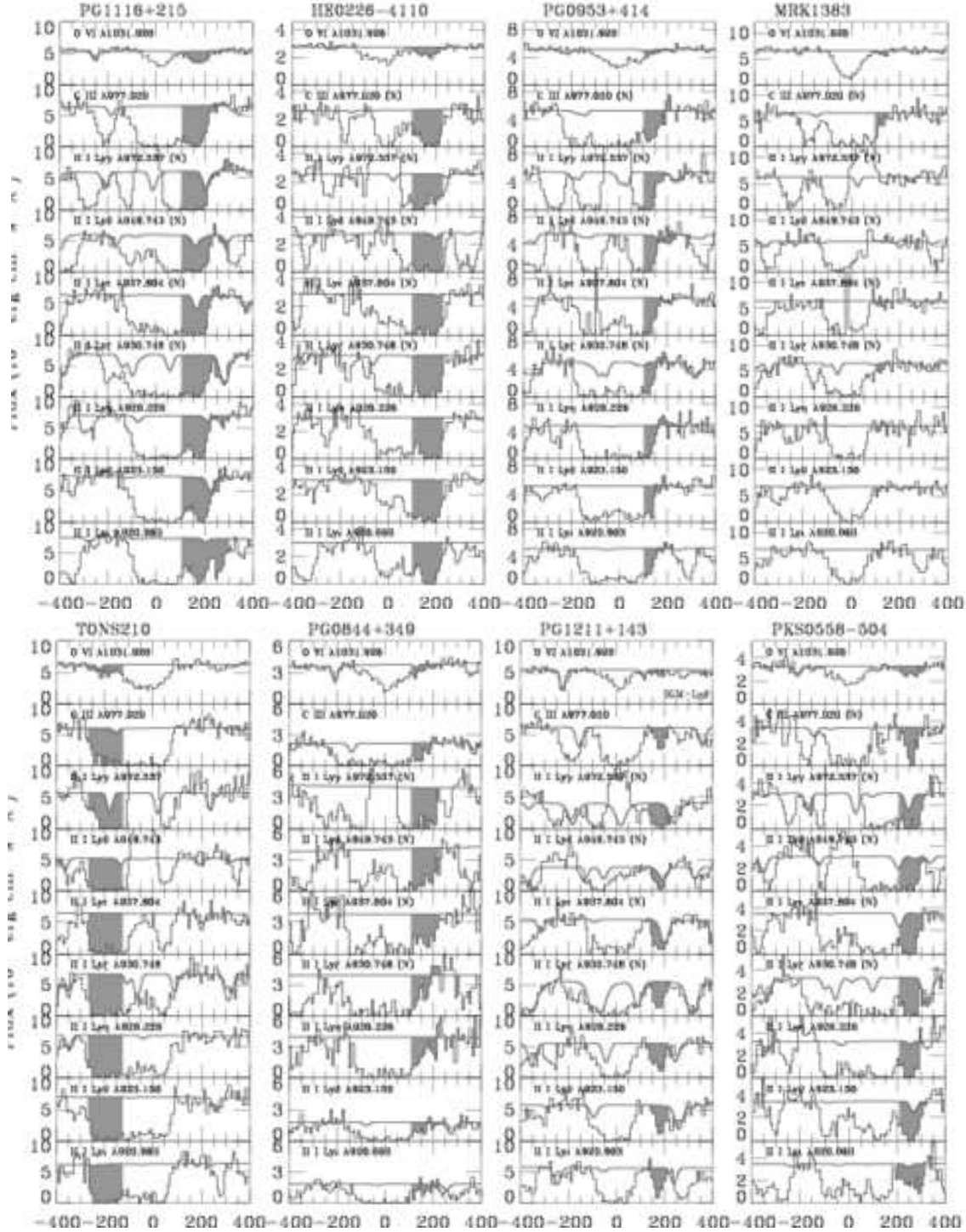


FIG. 2 CONT.—

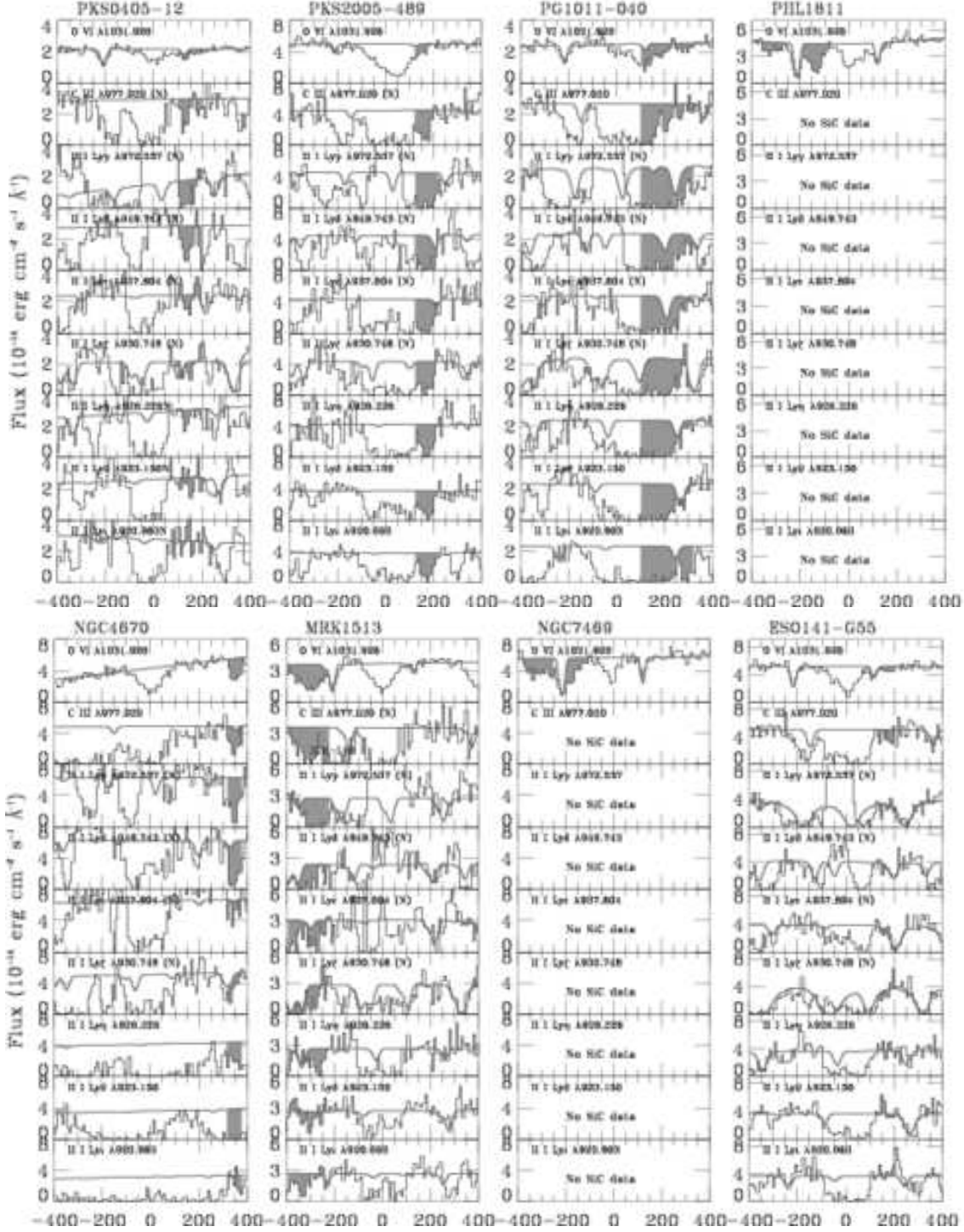


FIG. 2 CONT.—

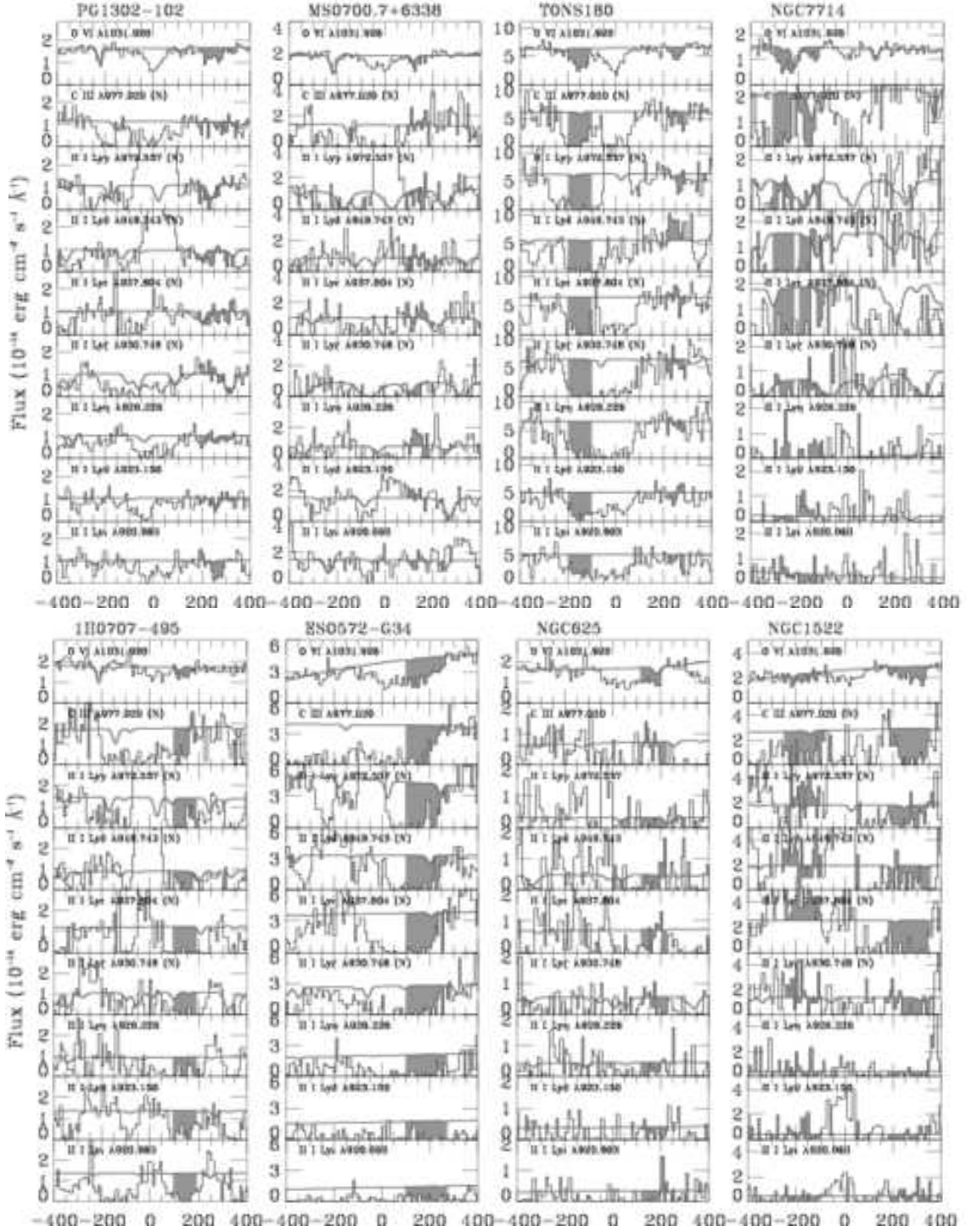


FIG. 2 CONT.—

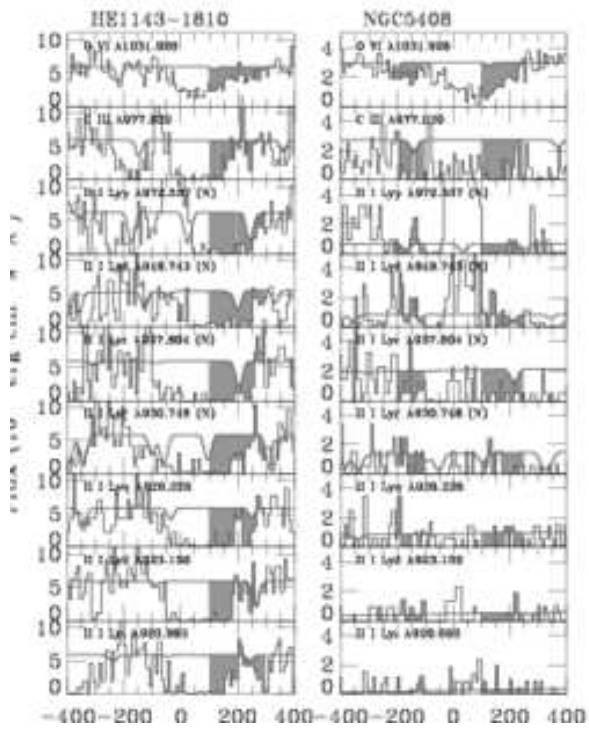


FIG. 2 CONT.—

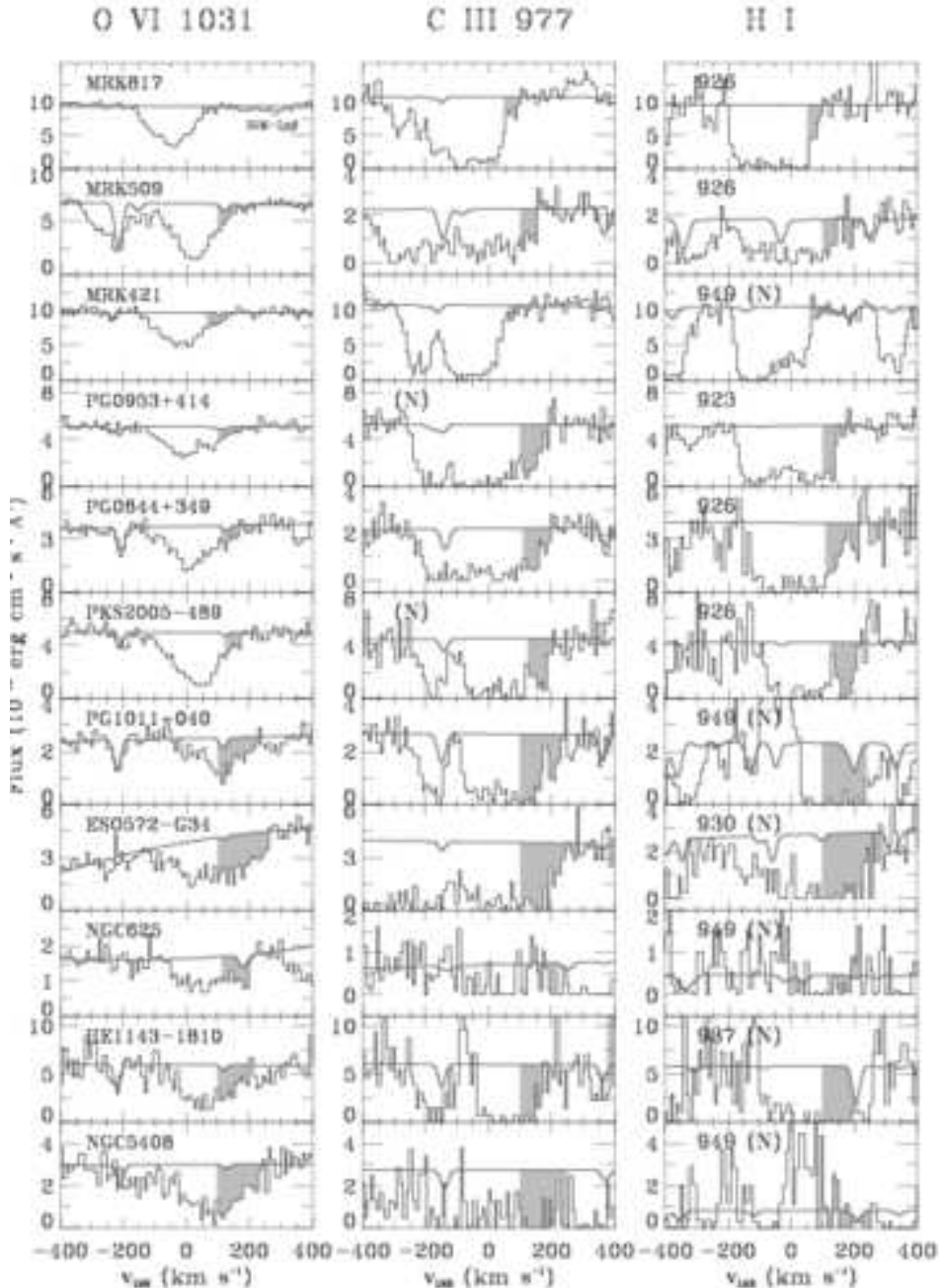


FIG. 3.— O VI, C III, and H I for all O VI-detected positive-velocity wings, presented in order of decreasing S/N.

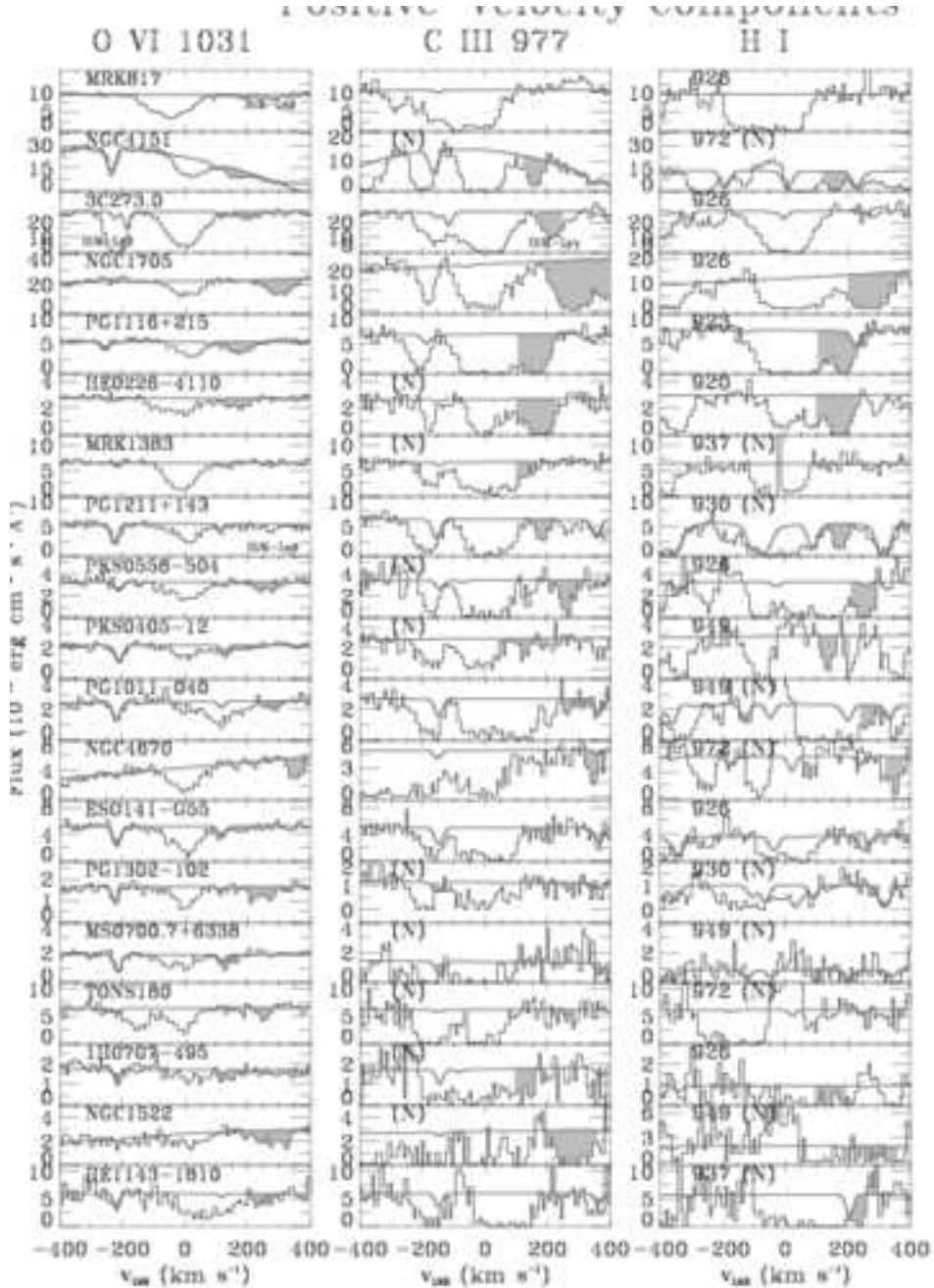


FIG. 4.— Same as Figure 3, but for all O VI-detected positive-velocity components.

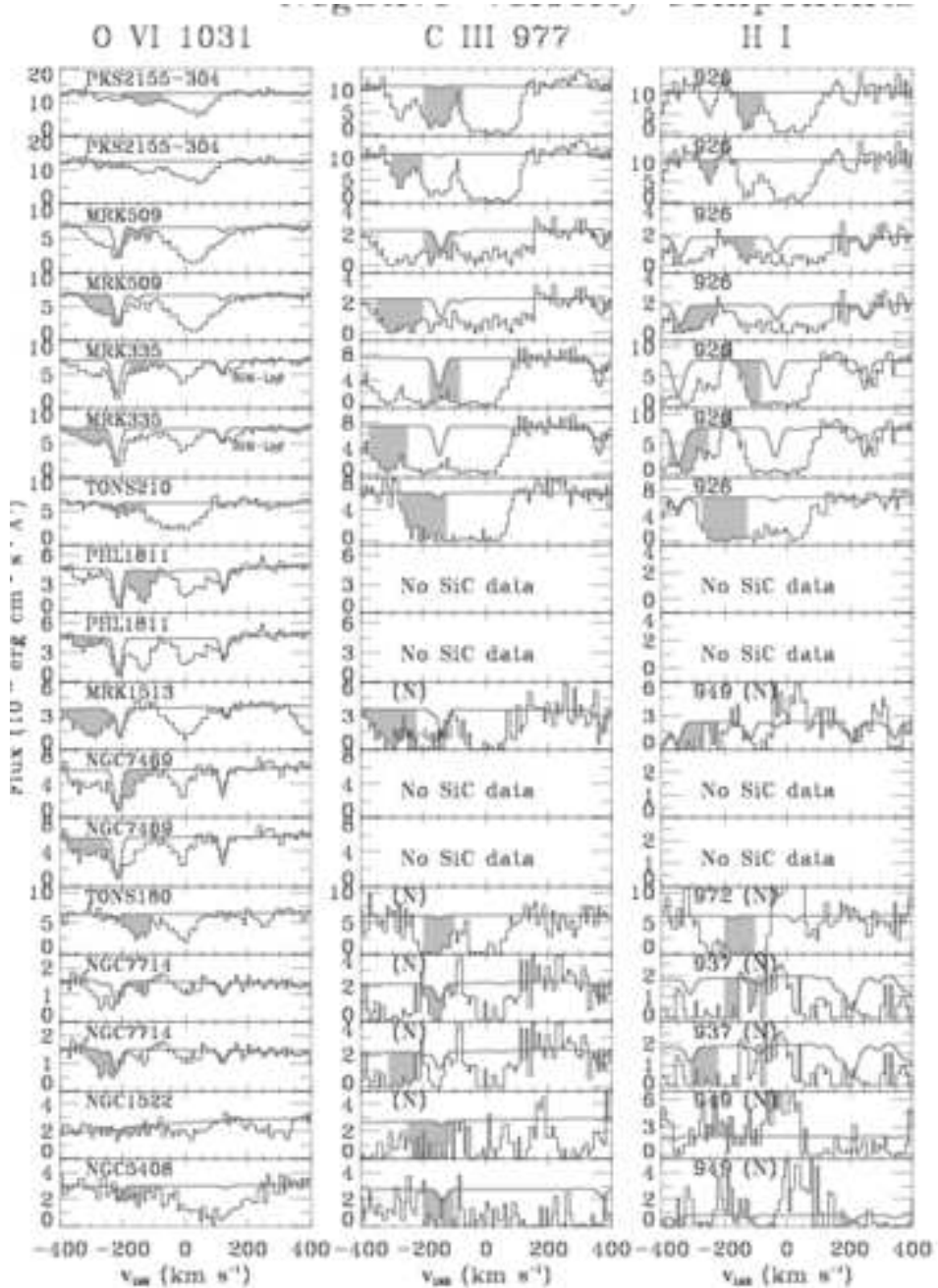


FIG. 5.— Same as Figure 3, but for all O VI-detected negative-velocity components.

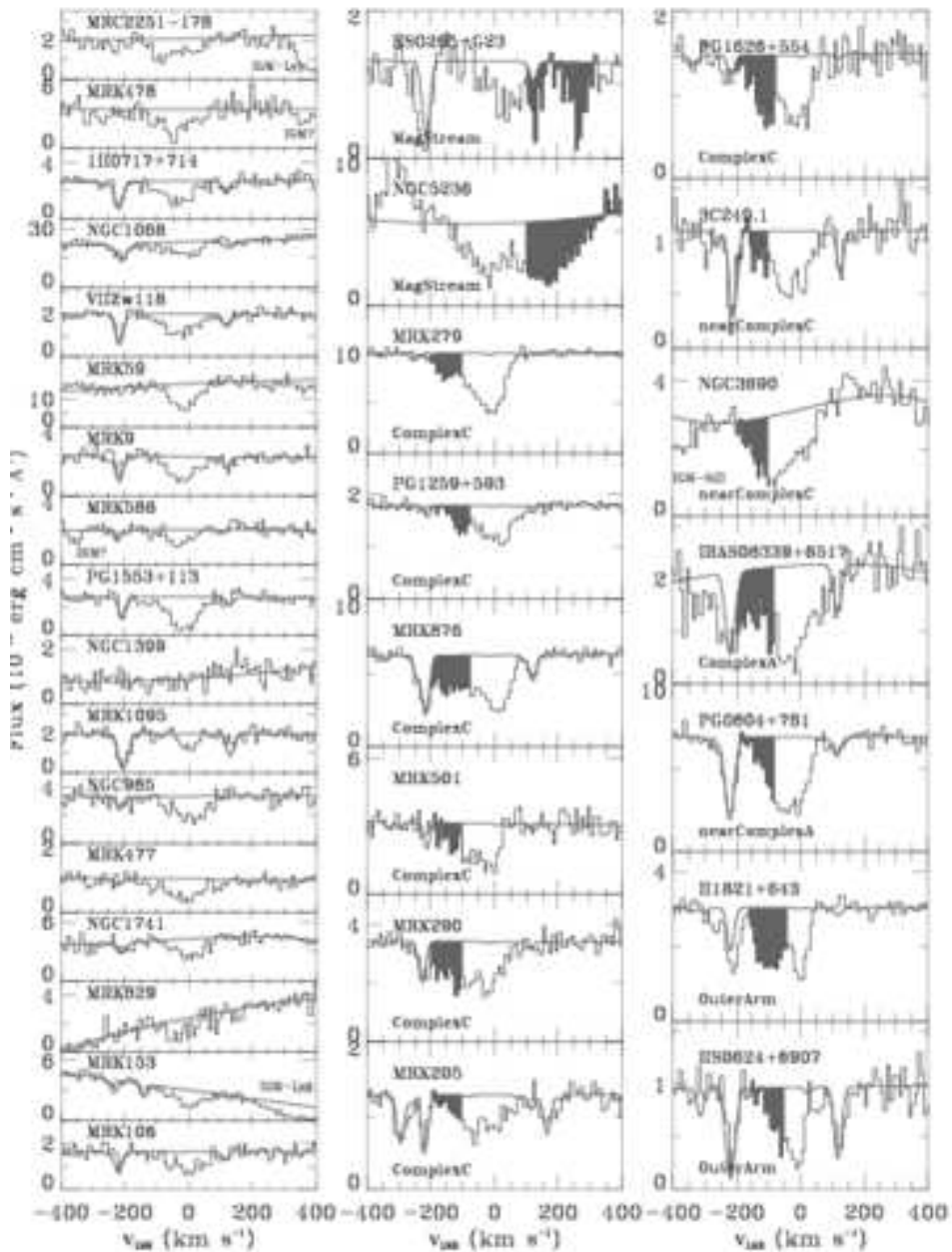


FIG. 6.— High-velocity O VI non-detections (left column) and high-velocity O VI associated with 21 cm-emitting HVCs (and hence excluded from our survey; right two columns).

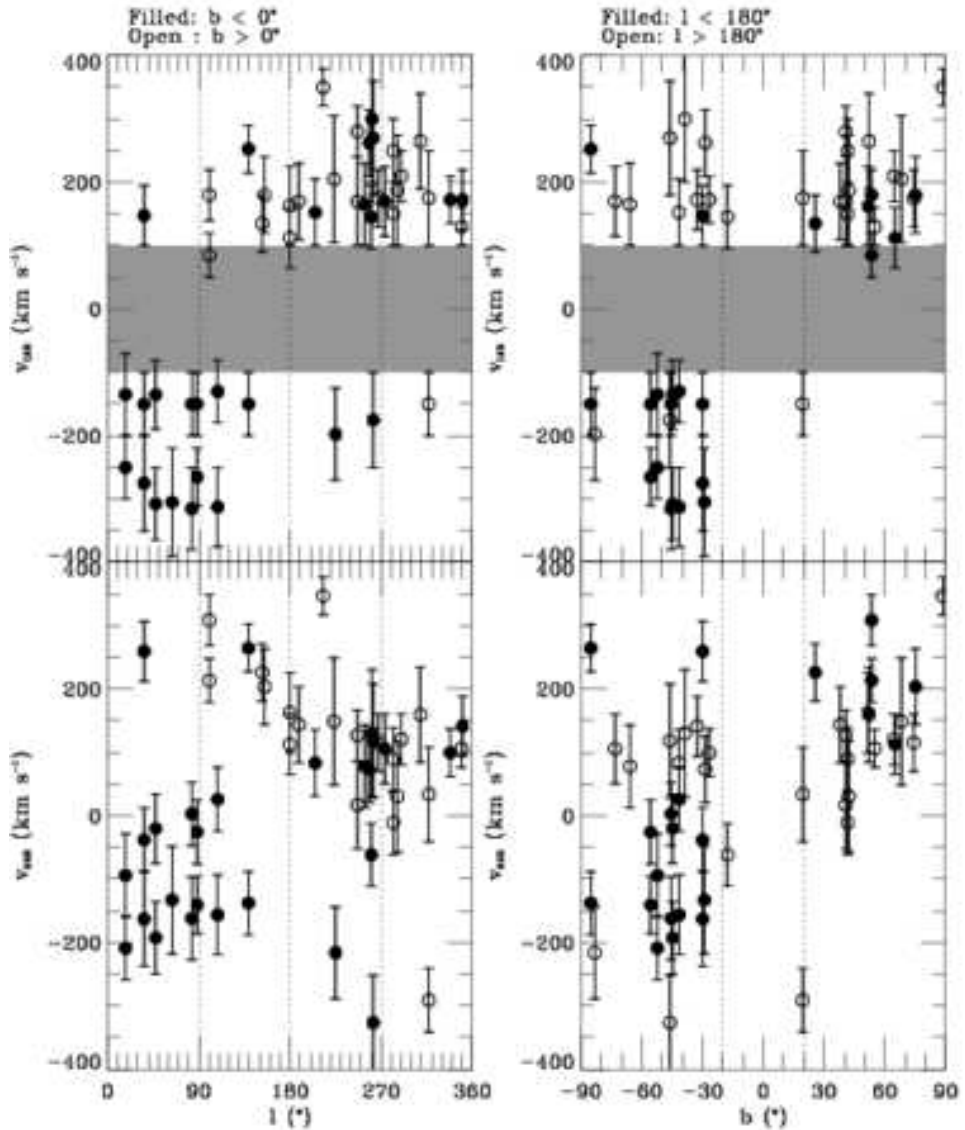


FIG. 7.— Kinematic analysis of high-velocity O VI absorbers as a function of location on the sky. In the top panels, v_{LSR} is plotted against Galactic longitude and latitude, respectively, with error bars denoting the minimum and maximum velocity of absorption. Shading denotes regions with $|v_{LSR}| < 100 \text{ km s}^{-1}$, by definition excluded from our search for high-velocity absorption. In the bottom panels, the velocities have been converted into the Galactic Standard of Rest reference frame.

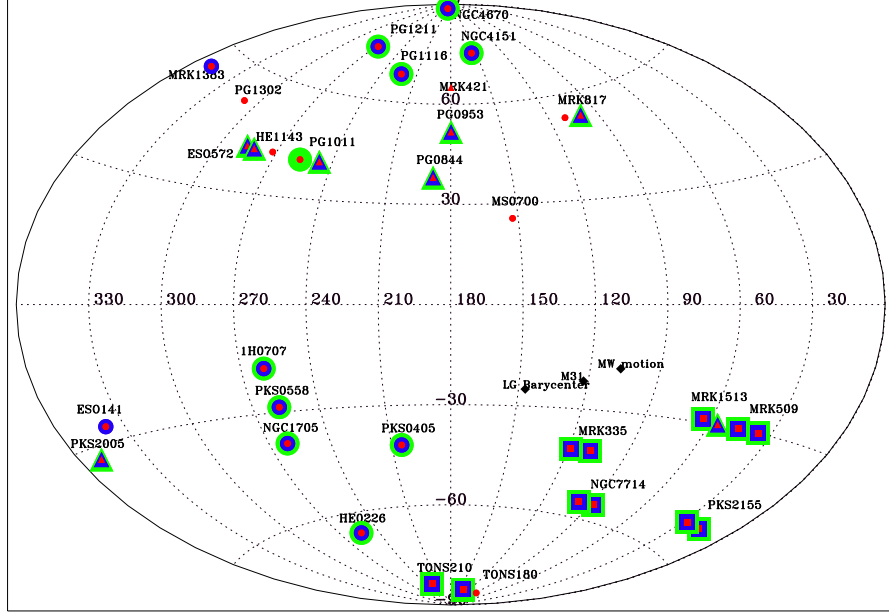


FIG. 8.— Map showing the prevalence of C III and H I absorption accompanying high-velocity O VI. For a given high-velocity absorber identified in O VI (red), a blue symbol shows a detection of C III, and a green symbol shows a detection of H I, in the same velocity range as the O VI. Circles denote positive-velocity components, triangles denote positive-velocity wings, and squares denote negative-velocity components. We have omitted cases where blends or poor data quality prevent us from knowing whether C III or H I is present. In six cases (PKS 2155, Mrk 335, NGC 7714, PG 1011, HE 1143, and Ton S180) there are two sets of symbols denoting two high-velocity absorbers; in one case (Mrk 509) there are three high-velocity absorbers shown. We include the following interesting locations: the Local Group barycenter ($l, b=147^\circ, -25^\circ$; Karachentsev & Makarov 1996), M 31 ($l, b=121.17^\circ, -21.57^\circ$), and the direction of the Milky Way's motion relative to the Local Group barycenter ($l, b=107^\circ, -18^\circ$; Einasto & Lynden-Bell 1982).

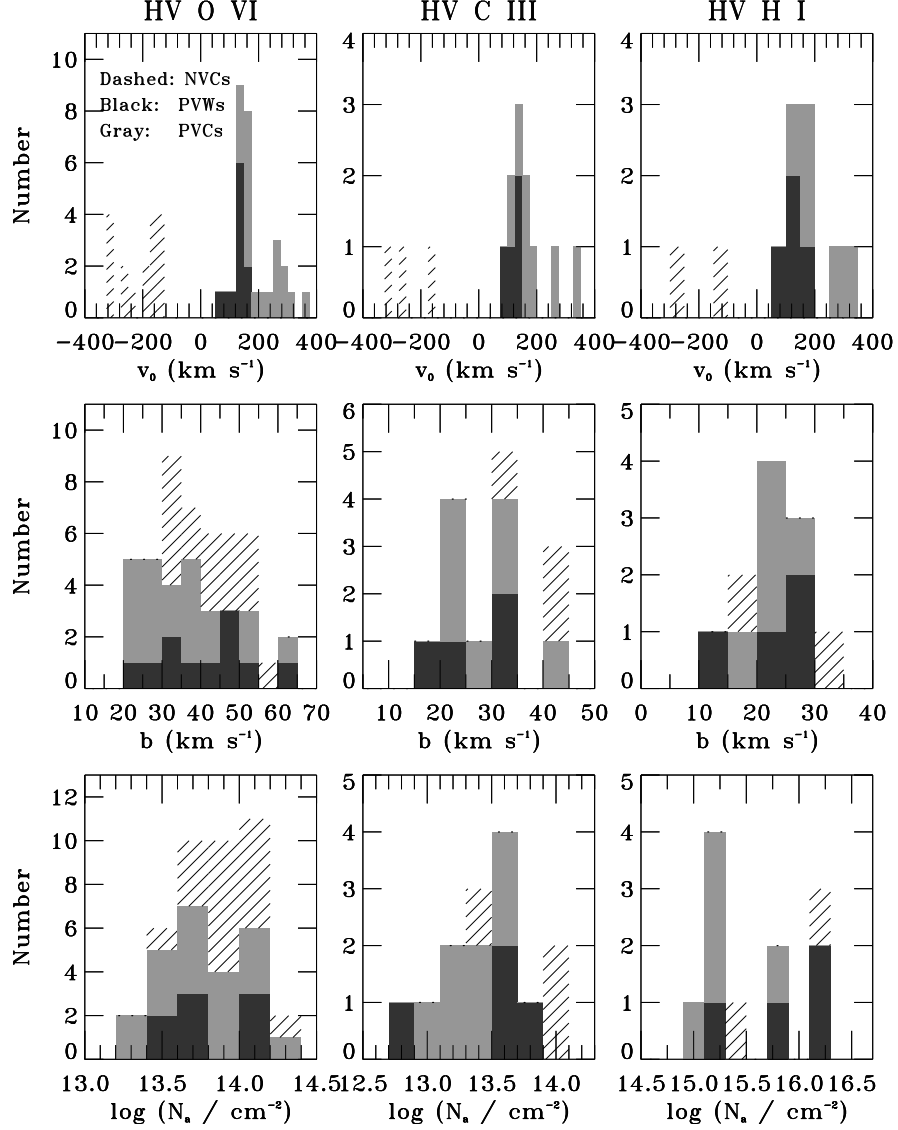


FIG. 9.— Distribution of properties of O VI HVCs (left column), C III HVCs (center column), and H I HVCs (right column). The top row shows the distributions of v_0 , the middle row shows the distributions of b , and the bottom row shows the distributions of $\log N_a$. Positive-velocity wings are shaded in black, positive-velocity components are in gray, and negative-velocity components are hatched. Only unsaturated C III and H I absorbers are included in this plot.

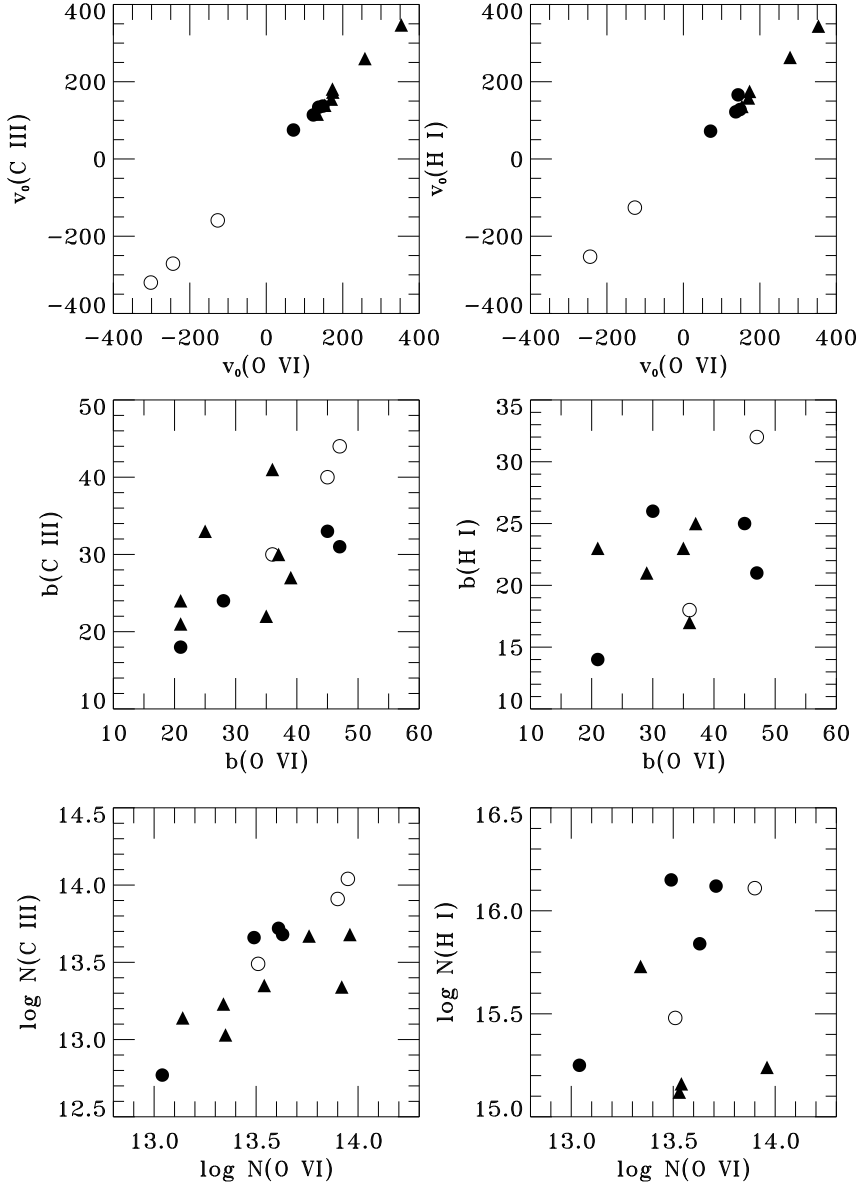


FIG. 10.—Scatter plots comparing properties of the high-velocity O VI absorbers (v_0 , b , $\log N$) with the corresponding properties in high-velocity C III absorbers (left panels) and high-velocity H I absorbers (right panels). Filled circles represent positive-velocity wings, open circles represent negative-velocity components, and filled triangles represent positive-velocity components. Only absorbers with unsaturated C III and H I lines are included in this plot.

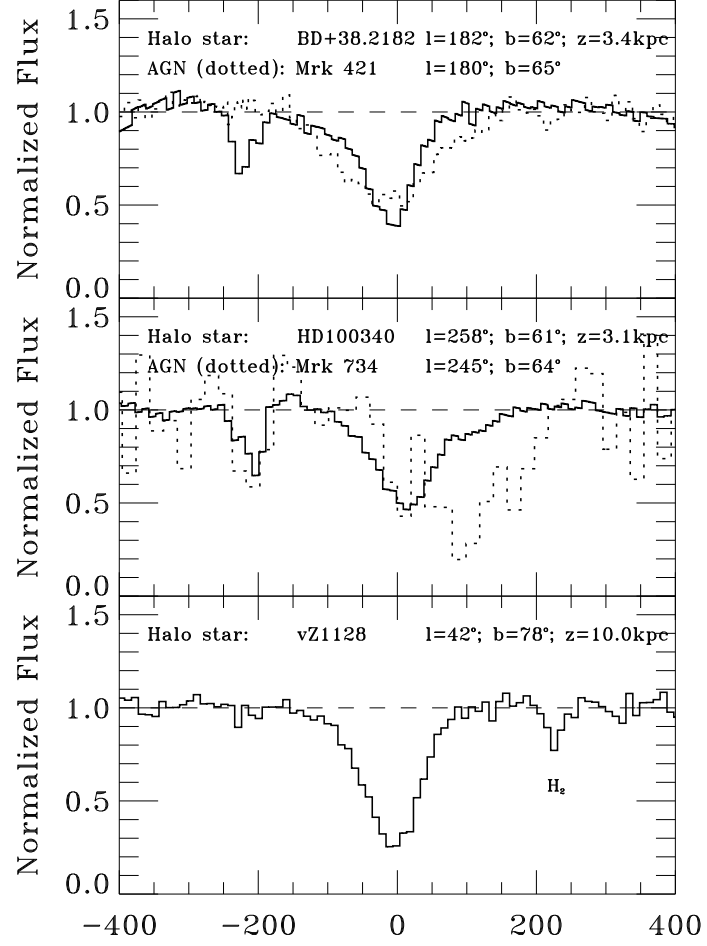


FIG. 11.— O VI profiles of three high- z halo stars and nearby extragalactic sight lines. Dashed lines show the continuum position. HD 100340 (solid line, middle panel) shows a weak O VI positive-velocity wing in the range 80 – 160 km s^{-1} , whereas BD+38.2182 and vZ 1128 do not. The dotted line in the top panel shows the O VI profile along the nearby sight line to AGN Mrk 421 (3.0° away from BD+38.2182). The dotted line in the center panel shows the O VI profile toward AGN Mrk 734 (7.0° away from HD 100340). The presence of high-positive-velocity absorption in the AGN spectra but not in the halo star spectra establishes that the wing absorption in these cases arises beyond the halo stars. The *negative-velocity wing* that appears to be present in the BD+38 2182 O VI spectrum is unrelated to the discussion of outflowing gas.

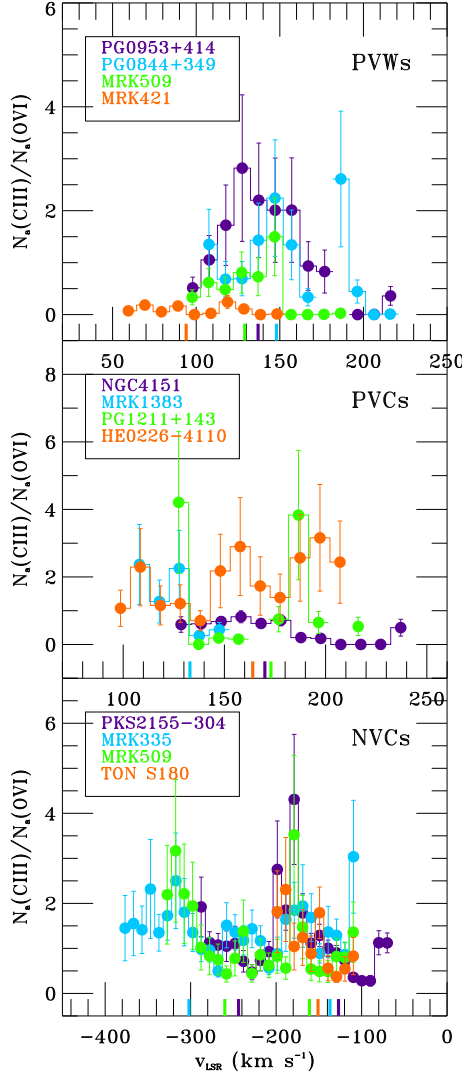


FIG. 12.— Dependence on velocity of the $N(\text{C III})/N(\text{O VI})$ ratio in positive-velocity wings (top), positive-velocity components (middle), and negative-velocity components (bottom). Each absorber is plotted using a unique color over the velocity range of high-velocity absorption. Absorbers showing little saturation in C III were included in this plot. Small vertical marks at the bottom each panel indicate the component center of each absorber. With some exceptions, these ratios show little slope with v_{LSR} . If the C III and O VI exist in the same gaseous phase, the observed ratios of between 0.1 and 4 imply a CIE temperature of $1.6\text{--}1.9 \times 10^5$ K, assuming solar abundances.

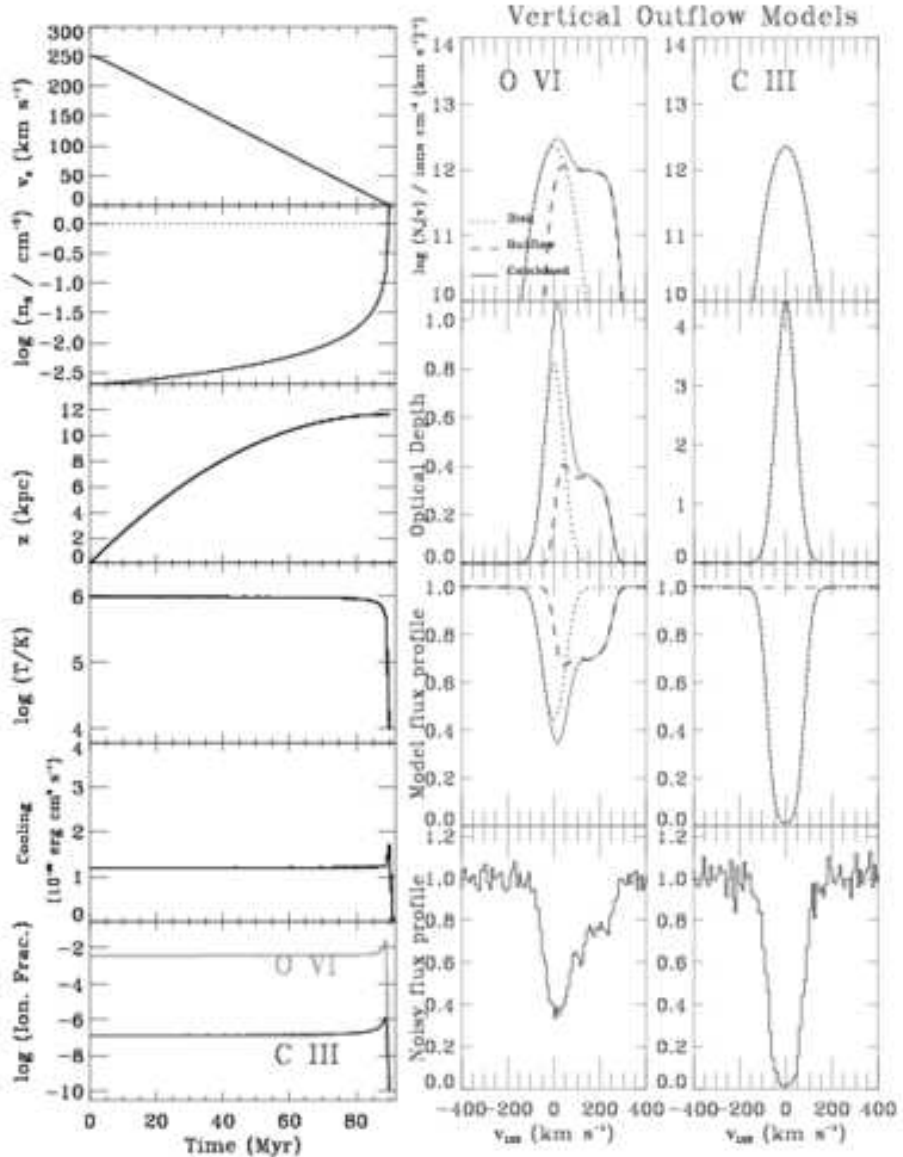


FIG. 13.— Results of modelling a radiatively cooling vertical Galactic outflow with dynamics dominated by the Galactic gravitational field, for the case $b=90^\circ$. This model run has $n_0 = 2.0 \times 10^3 \text{ cm}^{-3}$, $v_0 = 250 \text{ km s}^{-1}$, and $T_0 = 10^6 \text{ K}$. The left panels show the run of various physical properties of the flow with time in Myrs. The right panels show the predicted O VI and C III profiles, in column density per unit velocity, optical depth, flux after instrumental broadening, and flux with Poisson Noise introduced at a level of $S/N = 15$. The dashed line shows the outflow component, the dotted line shows a thick-disk component (Savage et al. 2003), and the solid line shows the sum of the two. The wing on the O VI profile traces the higher-velocity, higher-temperature stages of the outflow. Little C III exists at these temperatures in CIE, so our outflow modelling does not predict a wing on the C III profile.

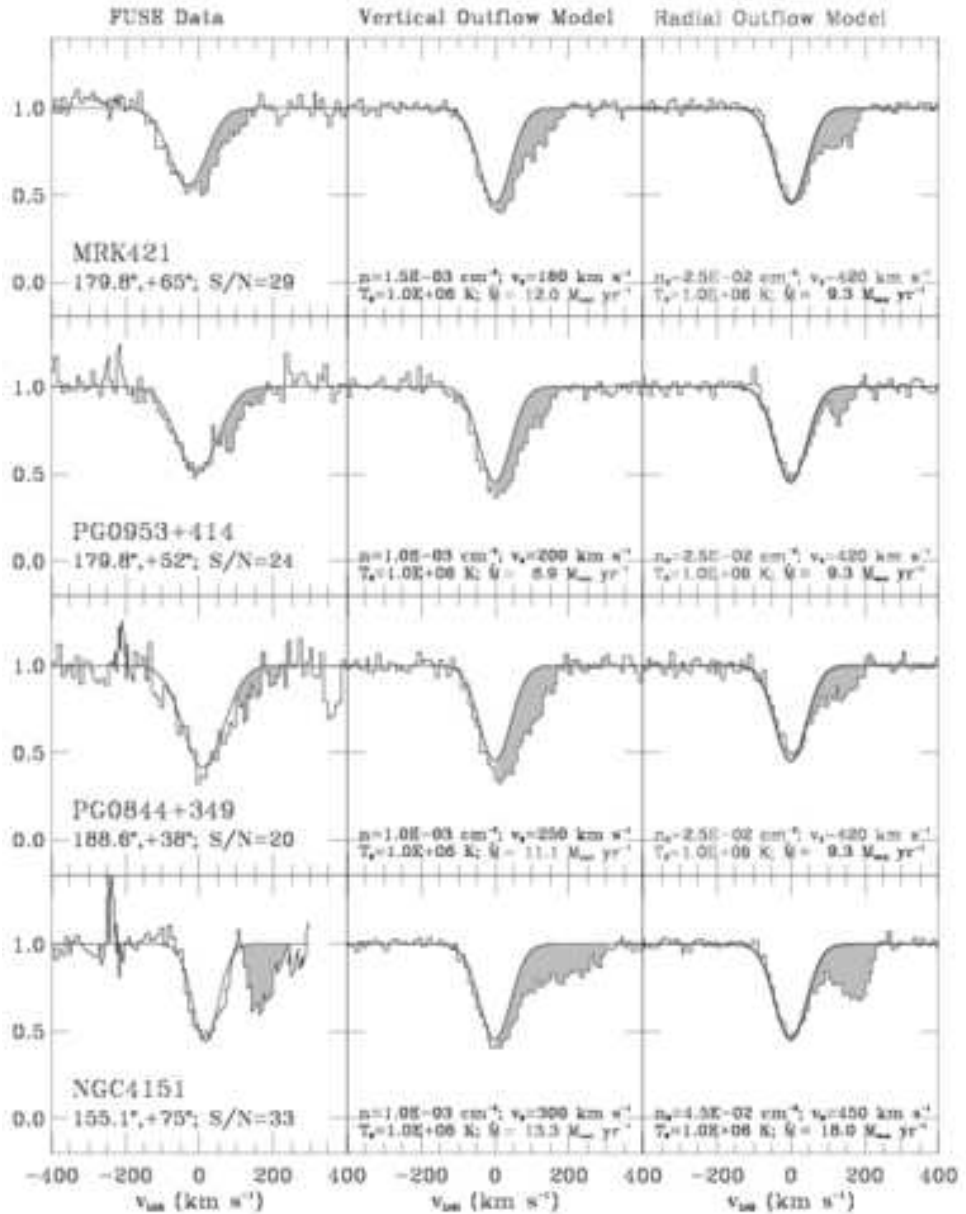


FIG. 14.— Comparison of four observed high-velocity O VI absorbers (left) near $l=180^\circ$ with the simulated results from vertical (center) and radial (right) outflow models. Noise has been added to the model profiles at the same level as in the data. In each panel, the smooth line shows the thick disk component, and the shading shows the residual, high-velocity absorption. The vertical outflow models produce broad positive-velocity wings, whereas the radial outflows produce narrower O VI absorption components, due to “velocity-crowding” projection effects.